A mechanistic model for the complex conductivity of clay materials. I. Theory

Philippe Leroy, Alexis Maineult, Aida Mendieta, Damien Jougnot

A mechanistic model for the complex conductivity of clay materials. I. Theory

Philippe Leroy[1,*], Alexis Maineult[2], Aida Mendieta[3], Damien Jougnot[4]

[1] BRGM, French Geological Survey, 45060 Orléans, France.

[2] Laboratoire de Géologie, Ecole Normale Supérieure / CNRS UMR 8538, PSL Research University, 75005 Paris, France.

[3] Université de Paris, Institut de Physique du Globe de Paris, 75005 Paris, France.

[4] Sorbonne Université, CNRS, EPHE, UMR 7619 METIS, 75005 Paris, France.

[*]Corresponding author, p.leroy@brgm.fr

Intended for publication in Geophysical Journal International

SUMMARY

Clay materials are ubiquitous in the Earth's continental and oceanic crusts. They are characterized by a large specific surface area, and, in contact with water, they have remarkable adsorption, catalytic and containment properties. Clay materials also exhibit a high electrical conductivity response associated with their large surface. However, sedimentary clay minerals have a complex microstructure and electrochemistry that are not fully understood and make the quantitative petrophysical interpretation of geoelectrical measurements difficult. In this study, we have developed a new mechanistic model to better understand and predict the complex conductivity of clay materials from their microstructure and electrical double layer properties. For the conductive component, our model considers ion electromigration in bulk water, clay electrical diffuse layer, and interlayer space, if any. Concerning polarisation, it takes into account ion back-diffusion in the Stern layer and in the interlayer space, if any, and also Maxwell-Wagner effect. Water and clay surface conductivities, formation factor, cementation exponent and sample electrically connected porosity can be extracted from the comparison of the model to experimental data. This study is a step forward to better understand and quantify the complex conductivity of clays observed during electrical and electromagnetic measurements, from laboratory to geological formation scales.

Keywords: Electrical properties, Induced polarisation, Microstructure.

47 Nomenclature

Symbol	Meaning	Unit
a_i^b	ion *i* activity in bulk water	dimensionless
α	empirical value to compute solid permittivity	$m^3\ kg^{-1}$
β_i^b	ion mobility in bulk water due to electro-migration	$m^2\ s^{-1}\ V^{-1}$
β_{eo}^d	mean ion electro-osmotic mobility in the diffuse layer	$m^2\ s^{-1}\ V^{-1}$
β_S	mobility of the counter-ions in the Stern layer	$m^2\ s^{-1}\ V^{-1}$
$\overline{\beta_i^b}$	ion mobility in bulk and distilled water due to electro-migration	$m^2\ s^{-1}\ V^{-1}$
B_i^d	ion *i* mobility in the diffuse layer with electro-osmosis	$m^2\ s^{-1}\ V^{-1}$
B_d	mean ion mobility in the diffuse layer with electro-osmosis (thin diffuse layer assumption)	$m^2\ s^{-1}\ V^{-1}$
$\widetilde{B_d}$	mean ion mobility in the diffuse layer with electro-osmosis around the aggregate (thin diffuse layer assumption)	$m^2\ s^{-1}\ V^{-1}$
c	volume fraction of conductive water	dimensionless
CEC	cation exchange capacity	meq g^{-1}
C_d	differential capacitance of the diffuse layer	F m^{-2}
C_i^b	ion *i* molar concentration	mol L^{-1} (M)
C_{salt}^b	salt molar concentration	mol L^{-1} (M)
C_{NaCl}^0	initial NaCl concentration in bulk water	mol L^{-1} (M)
C_{salt}^0	initial salt concentration in bulk water	mol L^{-1} (M)
$\overline{C_i^d}$	average ion concentration in the diffuse layer	mol L^{-1} (M)
$\overline{C_{i^{z_i+}}^b}$	cation concentration from dissolved minerals and montmorillonite interlayer space	mol L^{-1} (M)
$\overline{C_{j^{z_j-}}^b}$	anion concentration from dissolved minerals and montmorillonite interlayer space	mol L^{-1} (M)
χ_d	diffuse layer thickness	m
χ_{D}	Debye length	m
d	diameter of the spherical particle	m
d_k	effective diameter of the k^{th} aggregate	m
d_S	Stern layer thickness	m
δ_s	clay powder mass	g
δ_{sc}	main clay solid mass	g
δ_t^0	sample mass before evaporation	g
δ_t^1	sample mass after evaporation	g
D_i^b	ion *i* self-diffusion coefficient	$m^2\ s^{-1}$
$\overline{D_i^b}$	ion *i* self-diffusion coefficient in distilled (bulk) water	$m^2\ s^{-1}$
e	elementary (or electron) charge	C
e_c	aggregate eccentricity	dimensionless
ε	medium permittivity	F m^{-1}
ε_0	vacuum permittivity	F m^{-1}
ε_{in}	interlayer space permittivity	F m^{-1}

ε_s	solid permittivity	F m^{-1}
ε_w	liquid water permittivity	F m^{-1}
$\overline{\varepsilon_w}$	average permittivity of the diffuse layer and interlayer space	F m^{-1}
$\mathbf{E}$	applied electrical field	V m^{-1}
$\mathbf{E}_0$	initial applied electrical field	V m^{-1}
$f(d_k)$	aggregate size distribution of the k^{th} aggregate	dimensionless
f_Q	fraction of the counter-charge in the Stern layer	dimensionless
k_B	Boltzmann's constant	J K^{-1}
K_w	dissociation constant of water molecules	dimensionless
ϕ	mud porosity	dimensionless
ϕ_a	aggregate porosity	dimensionless
η_w	liquid water dynamic viscosity	Pa s
h_k	height of the k^{th} aggregate	m
$\mathbf{H}$	magnetic field strength	A m^{-1}
i	imaginary number	dimensionless
I	ionic strength	mol L^{-1} (M)
κ	inverse of the Debye length	m^{-1}
φ	electrical potential in the diffuse layer	V
φ_d	electrical potential at the *d*-plane	V
φ_m	average electrical potential in the diffuse layer	V
$\mathbf{J}_C$	conduction current density	A m^{-2}
$\mathbf{J}_D$	displacement current density	A m^{-2}
pH	potential of hydrogen ion in bulk water	dimensionless
q	mean charge of the counter-ions in the Stern layer	C
q_i	ion *i* charge	C
Q_0	mineral surface charge density	C m^{-2}
Q_0^e	edge surface mineral surface charge density	C m^{-2}
Q_0^b	basal surface mineral surface charge density	C m^{-2}
Q_β	Stern layer surface charge density	C m^{-2}
Q_d	diffuse layer surface charge density	C m^{-2}
Q_{EDL}	electrical double layer surface charge density	C m^{-2}
Q_V	aggregate excess of charge per unit pore volume	C m^{-3}
Q_V^0	excess of charge per unit Stern and diffuse layer volumes	C m^{-3}
Q_V^d	excess of charge per unit diffuse layer volume	C m^{-3}
Q_V^{in}	excess of charge per unit interlayer space volume	C m^{-3}
Θ_w^d	water volume fraction of the diffuse layer	dimensionless
L	depolarisation coefficient	dimensionless
m	cementation exponent of the clay aggregate	dimensionless
m_i^d	electro-osmotic effect on diffuse layer conductivity	dimensionless
mr_S	ion mobility ratio between in the Stern layer and distilled water	dimensionless

M	effect of the diffuse layer on Stern layer polarization	dimensionless
n_c	number of stacked sheets per particle	dimensionless
N	number of ion species in bulk and diffuse layer waters	dimensionless
N_A	Avogadro's number	mol^{-1}
N_{d_k}	Number of different sized aggregates	dimensionless
N_s	number of solid inclusions in the modelling	dimensionless
ν	empirical coefficient for temperature dependence of ion mobility	K^{-1}
pK_w	minus log of dissociation constant of water molecules	dimensionless
ρ_s	solid volumetric mass density	kg m^{-3}
$\sigma^{(1)}$	medium electrical conductivity	S m^{-1}
$\sigma_0^{(1)}$	medium bulk conductivity (excluding polarisation effect)	S m^{-1}
$\sigma_s^{(1)}$	"surface" conductivity due to Stern layer polarisation	S m^{-1}
$\sigma_w^{(1)}$	water conductivity	S m^{-1}
$\sigma_w^{b\,(1)}$	bulk water conductivity	S m^{-1}
$\sigma_w^{d\,(1)}$	diffuse layer water conductivity	S m^{-1}
S_{in}	surface area of the interlayer space	m^2
S_o	outer surface area of the clay particle	m^2
SS	total specific surface area of the clay particle	m^2 g^{-1}
SS_e	specific surface area of the edge surface	m^2 g^{-1}
SS_b	specific surface area of the basal surface	m^2 g^{-1}
SS_o	total outer specific surface area of the clay particle	m^2 g^{-1}
Σ_s^d	Surface conductivity of the diffuse layer	S
Σ_S	Surface conductivity of the Stern layer	S
t	time	s
t_{in}	interlayer thickness	m
τ	relaxation time of the spherical particle	s
τ_k	relaxation time of the k^{th} sized aggregate	s
T	absolute temperature	K
T_C	temperature in degree Celsius	°C
ϑ	surface area weighting coefficient	dimensionless
V_{in}	interlayer space volume	m^3
V_s	solid volume	m^3
V_{sc}	solid clay layer volume	m^3
V_{so}	weakly conductive other solid volume	m^3
V_S	Stern layer volume	m^3
V_t	sample volume	cm^3
V_w^d	volume of diffuse layer water	m^3
V_w^b	volume of bulk water	m^3
ω	angular frequency of the applied electrical current	rad s^{-1}

Ω_s	solid content in the sample	dimensionless
x	distance from the *d*-plane	m
ξ_c	solid volume fraction of the main clay mineral	dimensionless
z	mean valence of the counter-ions	dimensionless
z_i	ion *i* valence	dimensionless

(1) Followed by "*" means including displacement current.

1 INTRODUCTION

Clay minerals or clays are fine-grained materials (particle size below 2 μm) that are very common in geologic deposits, terrestrial weathering environments (e.g., regolith), and marine sediments (Sposito 1989). They have a high specific surface area (SSA), the highest known among major natural minerals (Leroy & Revil 2009). For instance, one gram of montmorillonite (Mt), which belongs to the smectite group, can cover a surface of roughly 800 m^2 (Tournassat & Appelo 2011). Unlike other high-SSA natural minerals such as zeolites and manganese and iron (hydr)oxides, clay minerals are frequently the main components of soils and extended sedimentary stratigraphic layers, making around 40% of the minerals in sedimentary rocks (Schroeder 2018).

Unique properties of clays are due to their microstructure – among them high adsorption capability, swelling, catalysis, plasticity when wet, and very low permeability (Grim 1962). These minerals are hydrous layer aluminosilicates, which form a diverse group constituting the greater part of the phyllosilicate family of minerals. Clays are mostly made of aluminum, silicon, and oxygen atoms interacting with water molecules on the mineral surface, sometimes with variable amounts of iron, alkali metals (e.g., Na^+ or K^+), and alkaline earth metals (e.g., Ca^{2+} or Mg^{2+}) (Tournassat *et al.* 2015). They have a layered structure containing an octahedral (O) alumina sheet sandwiched between two tetrahedral (T) silica sheets (case of Mt and illite) or a tetrahedral silica and octahedral alumina sheet (case of kaolinite) that are stacked to form a particle (Leroy & Revil 2004).

Clay minerals have remarkable adsorption properties reflected by their high cation exchange capacities (CEC), typically between 0.1 and 1.5 meq g^{-1} for, in ascending order, chlorite, kaolinite, illite and Mt (Revil & Leroy 2004). Isomorphic substitutions in the crystal are, e.g., the replacement of Al^{3+} by Mg^{2+} or Fe^{2+} ions in octahedral sheets or Si^{4+} by Al^{3+} or Fe^{3+} ions

in tetrahedral sheets with most of the substitutions occurring in the octahedral sheets for illite and Mt (Leroy *et al.* 2017b). Isomorphic substitutions are responsible for a high permanent negative surface charge mostly expressed on the basal clay surfaces (Bourg & Sposito 2011). This surface charge, conjointly with the high specific surface area of illite (typically 100-200 $m^2 g^{-1}$ compared to a kaolinite SSA of typically 10-20 $m^2 g^{-1}$) and Mt (typically 700-800 $m^2 g^{-1}$) (Revil & Leroy 2004), are at the origin of the high measured CEC of illite (~0.2-0.3 meq g^{-1}) and Mt (~0.7-1.5 meq g^{-1}) (Revil & Leroy 2004; Tournassat *et al.* 2015). Clays such as Mt also have swelling properties due to the presence of hydrated cations such as Na^+ ions adsorbed in the interlayer space between TOT layers (Massat *et al.* 2016) and catalytic properties because of their high reactive specific surface area (Ismadji *et al.* 2015). Clay minerals also have rheological properties and develop plasticity when wet because of a molecular film of water surrounding clay particles, but become hard, brittle and non-plastic upon drying or firing (Guggenheim & Martin 1995).

Clays play a major role in the terrestrial biogeochemical cycling of metal cations (e.g., K^+ or Ca^{2+}) and in the chemical homeostasis of the oceans (Sposito *et al.* 1999) because they are abundant in Earth's soil and subsurface and of their high chemical reactivity (regarding, e.g., adsorption and catalysis) (Sposito *et al.* 1999). These minerals also provide an efficient confinement environment for biomolecules and might have enhanced biochemical reactions to develop life during early life evolution on Earth (Yang *et al.* 2013) and possibly on Mars (Azua-Bustos *et al.* 2020). Due to clay rheological properties, shale beds (sedimentary rocks composed of very fine clay particles) have preserved a remarkable range of fossils, e.g., hard body parts, soft tissues, feathers, prints, and burrows (Petraglia *et al.* 2014). Therefore these clayey rocks provide records of Earth's evolutionary history and inspired Charles Darwin for his theory of evolution (Charlet *et al.* 2017). Clay minerals also provide indicators of the

evolution of aqueous conditions and possible habitats for life on ancient Mars (Bristow *et al.* 2018).

In addition, clays are used in a broad range of engineering processes, for instance as lubricants in oil industry (Udonne 2011), industrial catalysts for the synthesis of organic compounds (Nagendrappa 2011), and for pharmaceutical drug delivery (Viseras *et al.* 2010). Since the Neolithic period, clay minerals have also been employed for pottery (Vandiver *et al.* 1989). Special attention is currently devoted to the pharmacological functions of clays and their biomedical applications in pelotherapy, wound healing, regenerative medicine, antimicrobial, and dermocosmetics (Viseras *et al.* 2019). Natural and synthetic clays are also used as semi-permeable membrane barriers adsorbing metallic pollutants (Gehin *et al.* 2007), salt ions (water desalinisation (Ali *et al.* 2021)) and organic pollutants (Kausar *et al.* 2018) to improve the quality of water resources. They are also used as containers in landfills because of their confining properties towards industrial and domestic wastes (Malusis *et al.* 2003).

Clay-rich (argillaceous) rocks, including marls, shale, mudstone, argillite and claystone (herein referred to as clay rocks), are sedimentary formations with a very low permeability (typically between 10^{-23} and 10^{-17} m^2, see Neuzil 1994). The low permeability of clay rocks is a consequence of consolidated fine-grained sediments containing a large fraction of nanopores (Yven *et al.* 2007) with a loss of pore connectivity during diagenetic or metamorphic rock reactions (Charlet *et al.* 2017). Because of their confining properties, clay geological formations act as cap rocks above oil and gas ("carbonated" energies) (Li *et al.* 2006) and geothermal energy ("decarbonated" energy) (Guisseau *et al.* 2007) reservoirs. They are also frequently used for the geological storage of H_2 (energy "vector") (Liu *et al.* 2022), CO_2 (Busch *et al.* 2016) and high-level nuclear waste (Sellin & Leupin 2013). Smectite minerals can adsorb and store CO_2 in their interlayer space to mitigate greenhouse gas emissions (Bø Hunvik *et al.* 2021). The swelling of smectite minerals in contact with an aqueous solution

123 can also produce strong adverse effects in the extraction of oil and gas (Karaborni *et al.* 1996)
124 and of "green" geothermal energy (Xu *et al.* 2006), and is of major concern in civil
125 engineering due to quick clay landslides (Khaldoun *et al.* 2009).

126 When clay mineral is in contact with water, an electrical double layer (EDL) lies on the
127 mineral outer surface to compensate the usual negative surface charge not compensated by
128 interlayer cations (Bourg *et al.* 2007). Some clays like kaolinite can have a positive surface
129 charge in acidic conditions because of the adsorption of protons on surface oxygen (Tombacz
130 & Szekeres 2006). The clay EDL is made of a "compact" Stern layer with a solid-like
131 viscosity and containing mostly counter-ions and of a diffuse layer with a liquid-like viscosity
132 and containing an excess of counter-ions and a deficiency of co-ions (Leroy & Revil 2004).
133 The EDL controls the distribution and displacement of electrical charges on the surface of
134 clays because of the high surface charge magnitude and specific surface area of clays
135 (Tournassat & Steefel 2019). Therefore, clay EDL has a strong influence on clay electrical
136 conductivity (Waxman & Smits 1968).

137 In geophysics, electrical and electromagnetic methods are very sensitive to electrical charge
138 transport in clay materials, especially in the EDL at the interface between solid clay and bulk
139 pore water (e.g., Revil & Leroy 2001; Jougnot *et al.* 2010a; Qi & Wu 2022). Any perturbation
140 of chemical, electrical, hydrostatic and thermal nature in a geological system containing a
141 significant fraction of clays should be theoretically captured by these methods (Revil & Leroy
142 2004; Revil *et al.* 2005; Revil & Linde 2006). Notably, the electrical current injected into the
143 ground containing clay materials moves the electrical charges in the pore water, especially
144 those in the diffuse part of the clay EDL and in the stagnant part of the clay EDL (Stern
145 layer), which in turn influence ground electrical conductivity (ability of the medium to carry
146 electric current) (e.g., Revil 2012; Okay *et al.* 2014; Qi & Wu 2024). In the laboratory, a
147 tension typically ± 5V and a resulting weak electrical current typically in the mA range is

injected when investigating pluricentimetric samples (Zimmermann *et al.* 2008). In the field, considerably higher voltages and currents are typically injected into the ground depending on the depth of the investigation (Kemna et al. 2012). The measured electrical and magnetic fields and related conductivities and susceptibilities can thus be used to estimate the petrophysical, state and transport properties of clay materials in geological formations (Triantafilis & Lesch 2005; Glaser *et al.* 2023; Porté *et al.* 2023).

A main inherent drawback of the conventional direct current (DC) resistivity survey is its ambiguity in distinguishing between the effects of groundwater salinity, clay content, and pore space geometry (Binley & Kemna 2005; Binley & Slater 2020). Among the electrical and electromagnetic methods, one named "induced polarisation" (IP) is of particular interest for geophysicists due to its increasing sensitivity to subsurface processes over the last 20 years (Kemna *et al.* 2012; Binley *et al.* 2015). The induced polarisation method is related to the reversible "storage" of electrical charges in porous media (Revil & Skold 2011). It was discovered more than 100 years ago by Conrad Schlumberger (as far as we know). After cutting the electrical current injected into the ground containing sulphide ores, Schlumberger observed that the related voltage did not disappear immediately and instead decreased slowly with time (Schlumberger 1920). Integrating the measured voltage in excess over the time after switching off the current allows estimating the chargeability of the investigated porous medium (Pelton *et al.* 1978). In the case of clay materials, the chargeability is sensitive to the excess of electrical conductivity in the clay EDL compared to in bulk water, which is responsible for clay "surface" conductivity controlled by clay microstructural and electrochemical properties (Leroy & Revil 2009; Leroy *et al.* 2017b; Revil *et al.* 2023). The IP method gives therefore access not only to the DC ("zero frequency") conductivity or resistivity but it also gives access to the chargeability of the investigated clayey medium (Revil & Florsch 2010; Revil 2012; Qi & Wu 2024). These physical quantities, due to their

dependence on clay pore water and surface conductivity, can deliver important information on the petrophysical properties of clay materials. These properties are, for instance, mineralogy, pore structure, water and clay contents, and transport properties including ion diffusivity and rock permeability (Jougnot et al. 2009, 2010b; Revil & Florsch 2010; El Alam et al. 2023; Revil et al. 2023).

The spectral induced polarisation (SIP) method belongs to the broader family of IP methods. Rather than switching off and on the injected current, a sinusoidal, low-frequency (typically in the mHz to kHz frequency range) electrical current is injected into the ground and the resulting voltage is measured (Marshall & Madden 1959). There are different ways of doing TDIP and SIP measurements in the laboratory and in the field. In the case of the Wenner alpha configuration, two current electrodes are used to inject the current and two potential electrodes located between the current electrodes and at equal separation distance are used to measure the resulting voltage in the investigated porous medium (e.g., Martin *et al.* 2020). Other frequently employed configurations are dipole-dipole, pole-dipole or Wenner-Schlumberger ones (Aizebeokhai & Oyeyemi, 2014).

During SIP measurements on clay materials, the magnitude of the measured voltage depends on ion fluxes induced by the imposed electrical field in the pore water especially on those in the clay diffuse layer and in the clay Stern layer (ion electromigration processes) (e.g., Leroy & Revil 2009; Okay *et al.* 2014). The measured phase-shift between injected current and measured voltage depends on ion counteracting diffusion fluxes to reestablish their distribution at thermodynamic equilibrium (Fig. 1) (e.g., Lyklema *et al.* 1983; Grosse & Delgado 2010). Indeed, when the frequency of the injected sinusoidal current is sufficiently low (typically below 1 kHz), the EDL polarizes (i.e. counter-ions in the EDL have time to electromigrate tangentially to the particle surface) to accumulate on one side of the particle, and to diffuse back to their initial position (Fig. 1a, Schwarz 1962). These ion movements,

198 which can be characterized by a relaxation time, thus create a complex surface conductivity
199 increasing the electrical conductivity of the medium (e.g., Leroy *et al.* 2008; Leroy *et al.*
200 2017a). When the frequency of the injected sinusoidal current is higher (typically above 1
201 kHz), there is a charge build-up at the boundary between two phases presenting different
202 conductivities and permittivities, like solid clay and water, responsible for another
203 polarisation mechanism, Maxwell-Wagner polarisation, and increasing the electrical
204 conductivity of the medium (de Lima & Sharma 1992). Nanoporous clay materials are
205 characterized by a broad distribution of relaxation times due to Stern layer polarisation
206 influencing in particular medium and high-frequency SIP measurements (Leroy & Revil
207 2009).

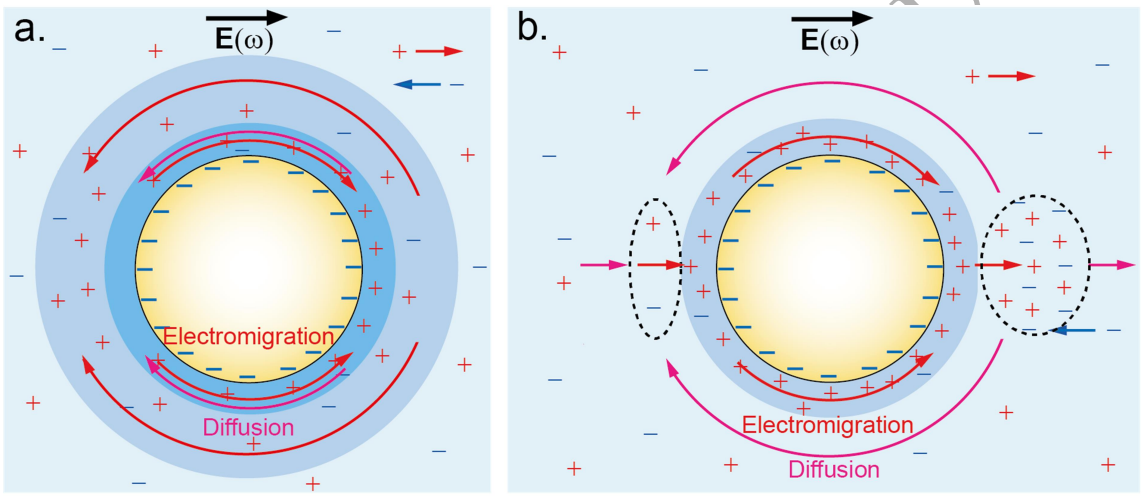

208

209 **Figure 1.** Sketch of EDL polarisation at low frequencies of the injected current for a
210 negatively charged particle. Model of Lyklema *et al.* (1983) (generalized Schwarz model)
211 showing the capacitive effect of the polarized thin layer usually assumed to be the Stern layer
212 (surface diffusion processes) (a., modified from Leroy *et al.* 2017b). Model of Grosse &
213 Delgado (2010) showing the formation of ion clouds in excess and deficiency outside the
214 EDL compared to in the surrounding electrolyte due to EDL (here diffuse layer) polarisation
215 (concentration polarisation, volume diffusion processes) (b., modified from Grosse &
216 Delgado 2010).

217 Petrophysical models have been developed to understand quantitatively SIP laboratory and
218 field IP measurements on clayey media. For instance, Vinegar & Waxman (1984) developed a

petrophysical SIP model for shaly sands based on an equivalent circuit model. Following Waxman & Smits (1968), their model assumes that the measured real part of the complex conductivity, the measured in-phase conductivity, can be understood quantitatively considering two conductances in parallel, one associated with electromigrating ions in the bulk pore water and one associated with electromigrating cation counter-ions on the clay surface. Following the membrane polarisation model of Marshall & Madden (1959), they considered in addition two conductances in series, one related to clay counter-ion displacement in clay-free zones and one related to electrolyte blockage by the clay-site membranes, to explain imaginary, quadrature conductivity measurements on shaly sands between 1 Hz and 1 kHz. In the model of Vinegar & Waxman 1984, the in-phase and quadrature (or out-of-phase) conductivities depend on Q_V, which is the excess of counter-charge (canceling clay surface charge) per unit pore volume and is calculated from the measured porosity and clay cation exchange capacity. The SIP model of Vinegar & Waxman (1984) is elegant and easy to use but its main drawback is, in our opinion, its establishment at the macroscale of the centimetric sample that does not allow it to explicitly consider clay microstructure and EDL properties. de Lima & Sharma (1992) developed mechanistic SIP models for clay materials considering explicitly Stern layer (Schwarz 1962) or diffuse layer (Fixman 1980) polarisation and Maxwell-Wagner polarisation (Sen *et al.* 1981). The SIP model of de Lima & Sharma 1992 is more physical and more difficult to handle than the SIP model of Vinegar & Waxman (1984). In our opinion its main drawback is its inability to capture clay microstructure with very elongated interacting clay particles on the contrary to the spherical clay particle considered in the model of de Lima & Sharma (1992). Most of the following SIP models for clay materials were inspired by the works of Vinegar & Waxman (1984) and de Lima & Sharma (1992) (e.g., Leroy & Revil 2009; Jougnot *et al.* 2010a; Revil 2012; Okay *et al.* 2014; Weller *et al.* 2015; Leroy *et al.* 2017b; Revil *et al.* 2023; Qi & Wu

2024). For instance, Leroy *et al.* (2017b) considered a Stern layer polarisation model for dispersed clay particles interacting with each other and forming aggregate. However, they did not consider Maxwell-Wagner polarisation. In addition, the role of the interlayer space of Na-montmorillonite (Na-Mt) containing hydrated and mobile Na^+ cations (Bourg *et al.* 2003) on clay conduction and polarisation during SIP measurement was not investigated in the previously reported works. In our knowledge, most of the current SIP models are not considering explicitly clay microstructure and EDL properties. The microstructural and electrical properties of the different components of the clay material, e.g., bulk pore water, diffuse layer, Stern layer, and interlayer space, are not clearly described.

In this study, we propose a new mechanistic model to interpret SIP measurements on unconsolidated clay materials (e.g., muds) as a function of salinity and temperature from clay microstructural and EDL properties. Our model is an extension of the SIP model of Leroy *et al.* (2017b). It considers bulk pore water and diffuse layer conductivities as well as Stern layer and Maxwell-Wagner polarisations including the contribution of the interlayer space of Na-Mt, which both were neglected in Leroy *et al.* (2017b) due to the low concentration of clay particles in the suspension (less than 60 g of clay powder per liter of electrolyte). Porosity, cementation exponent, electrical formation factor, surface conductivity and water conductivity can be extracted from our model compared to experimental data in order to better understand the electrical properties of clay materials and to test the assumptions of SIP petrophysical models developed at larger scale (e.g., Weller *et al.* 2013). Section 2 of our manuscript explains the microstructural and electrochemical properties of the main clay minerals, i.e. kaolinite, illite and montmorillonite clays. Section 3 presents the theory of our mechanistic SIP model that is compared to the experimental data of *Mendieta et al.* (2021) in the companion paper by Maineult *et al.* (2024).

2 CHARACTERISTICS OF KAOLINITE, ILLITE AND MT PARTICLES

2.1. Microstructural properties

Clay minerals are characterized by a wide variety of mineralogies, sizes and shapes, and heterogeneities in their surface properties (the edge surfaces behave differently than the basal surfaces) (Tombacz & Szekeres 2006; Brigatti *et al.* 2013). Clay particles (or tactoids) are a stack of platelets that are very elongated (Tournassat *et al.* 2015). These particles have therefore a high aspect ratio with a thickness considerably smaller than length for illite and Mt particles. Typical dimensions of clay platelets and particles are indicated in the following text.

The chemical formula of kaolinite is $Al_2Si_2O_5(OH)_4$ (Grim 1962). A kaolinite particle is a stack of several silica tetrahedral (T) and alumina octahedral (O) sheets linked by hydrogen bonds (1:1 clay). The thickness of a TO sheet is ~7 Å (Fig. 2a) and its length is typically between 200 and more than 1000 nm (Fig. 3a) (Tournassat *et al.* 2015). The specific surface areas (SSA) of the TO platelets (or layers) can be estimated from crystallography (Leroy & Revil 2004). Indeed, a square TO platelet with a thickness of 7.2 Å, a length of 500 nm and a solid volumetric density of 2.62 g cm^{-3} (Hassan *et al.* 2006) has a total specific surface area of about 1063 m^2 g^{-1} from which the edge surface share is about 3 m^2 g^{-1} and the basal surface share is about 1060 m^2 g^{-1}. According to the previous calculation and Hassan *et al.* 2006 and Tournassat *et al.* 2015, the edge specific surface area of a TO platelet is about 2-7 m^2 g^{-1} and the basal specific surface area of a TO platelet is about 1060-1070 m^2 g^{-1}. The edge SSA of individual TO layers is therefore roughly 150 to 500 times lower than their basal SSA. In addition, a kaolinite particle is considerably thicker and larger in average than an illite and Mt particle (Fig. 3). Kaolinite particle thickness is typically from less than 7 nm to more than 140 nm (Tournassat *et al.* 2015). The number of stacked TO layers of a kaolinite particle can therefore range from 10 to more than 200.

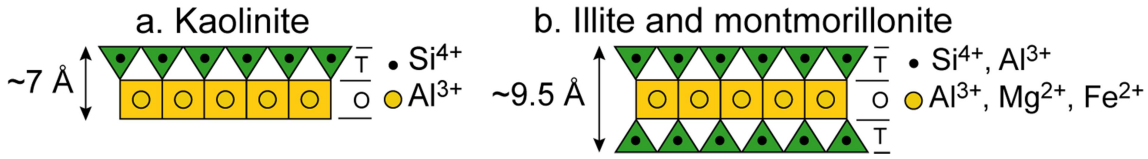

293

294 **Figure 2.** Sketch of (a.) kaolinite, and (b.) illite and Mt platelets (modified from Leroy &
295 Revil 2009).

296

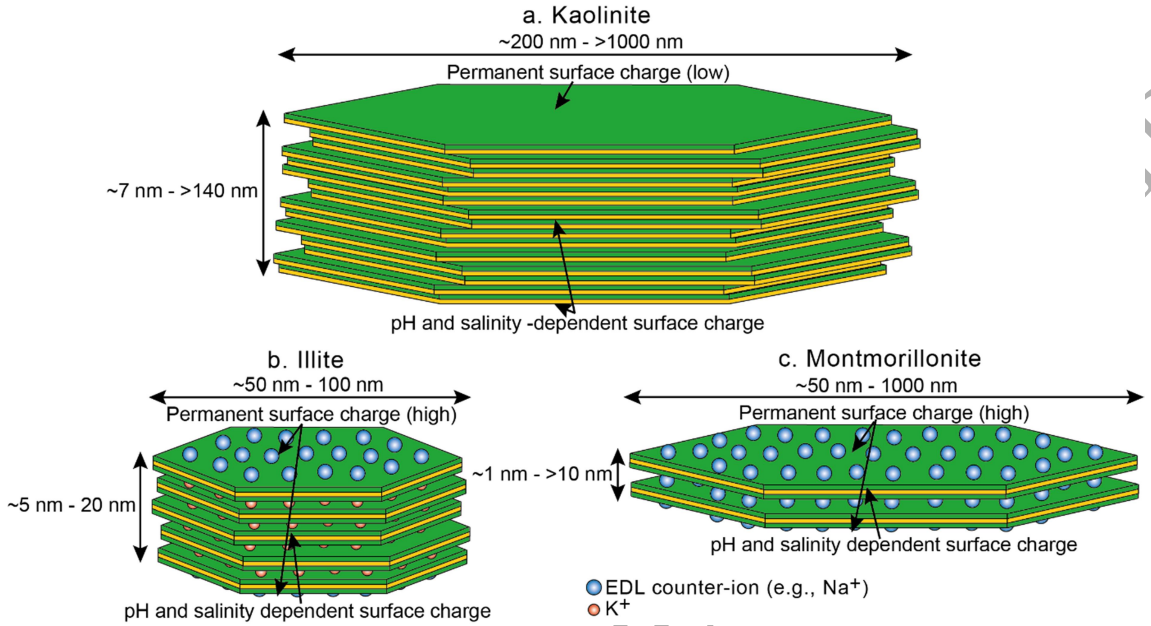

297

298 **Figure 3.** Sketch of (a.) kaolinite, (b.) illite and (c.) Mt particles (modified from Tournassat *et*
299 *al.* 2015).

300 The chemical formula of illite is $(K,H_3O)(Al,Mg,Fe)_2(Si,Al)_4O_{10}[(OH)_2,(H_2O)]$ and the
301 chemical formula of Mt is $(Na,Ca)_{0.33}(Al,Mg)_2Si_4O_{10}(OH)_2{\cdot}n(H_2O)$ (Grim 1962). Illite and Mt
302 particles are stacks of TOT sheets of thickness ~9.5 Å (Fig. 2b) and length between 50 and
303 100 nm for illite (Fig. 3b) and between 50 and 1000 nm for Mt (Fig. 3c) (Tournassat *et al.*
304 2015). TOT sheets exhibit a permanent negative charge on their basal surfaces and are bonded
305 by non-solvated cations (e.g, K^+) for illite and fully solvated cations (e.g., Na^+ and/or Ca^{2+})
306 for swelling clays such as Mt (2:1 clays) (Tournassat *et al.* 2015). From crystallographic
307 consideration, it can be estimated that the total specific surface area of a TOT layer is about
308 780 $m^2\ g^{-1}$, from which the edge surface share is about 10-30 $m^2\ g^{-1}$ and the basal surface

share is about 750-770 m^2 g^{-1} (Leroy *et al.* 2015). The edge SSA of individual TOT layers is therefore roughly 20 to 80 times lower than their basal SSA. The SSA of clay layers are thus dominated by the contribution of the basal surfaces, as the edge SSA represents only a minor part of the total SSA. Furthermore, illite particle thicknesses are typically from 5 nm to 20 nm and Mt particle thicknesses are typically from 1 nm to above 10 nm (Tournassat *et al.* 2015). Therefore, Mt particles are more elongated than illite particles. Illite particles typically consist of 5 to 20 stacked TOT layers. The TOT layers of Mt particles can become completely delaminated. The number of TOT layers per Mt particle rarely exceeds 10 in water (Tournassat & Appelo 2011). The number of TOT layers per Mt particle increases with decreasing water chemical potential and also tends to increase with the valence of the counter-ion in the interlayer space (Tournassat *et al.* 2015). According to viscosity and light-transmission experiments, Na-Mt dispersions in pure water contain particles made up of 1-2 TOT layers, whereas Ca-Mt or Mg-Mt dispersions in pure water contain particles made up of 6-10 TOT layers (Schramm & Kwak 1982).

The total SSA of a kaolinite particle, typically 10-20 m^2 g^{-1} (where the edge surface shares around 15% of it, around 1.5-3 m^2 g^{-1} (Hassan *et al.* 2006)), is considerably smaller than the total SSA of an illite or Mt particle, which is typically between 100 and 200 m^2 g^{-1} for illite and between 750 and 800 m^2 g^{-1} for Na-Mt (Revil & Leroy 2004; Hassan *et al.* 2006; Tournassat & Appelo 2011; Tournassat *et al.* 2015). Due to the irregular morphology of clay mineral layers, the edge surfaces of different layers in a single particle may be misaligned. Moreover, translational and rotational disorder between adjacent layers makes the structure turbostratic at the scale of individual clay mineral particles. Clay minerals have different morphologies: kaolinite and well-crystallized illite have a tendency toward hexagonal and elongated hexagonal morphologies, respectively, whereas Mt and less well-crystallized illite have mostly irregular platy or lath-shaped morphologies (Fig. 4).

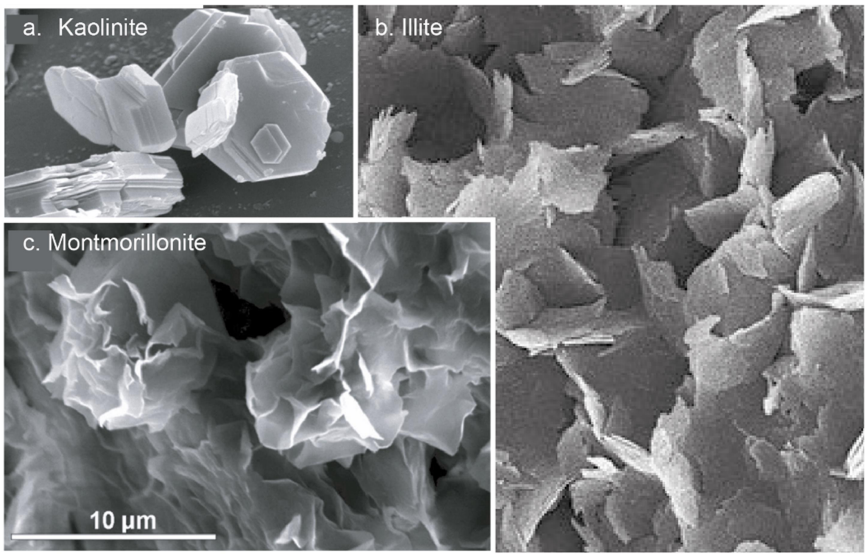

334

335 **Figure 4.** Scanning electron microscopy (SEM) images of dried kaolinite (a., modified from
336 Christidis 2010), illite (b., modified from Mc Bride 2012), and Mt (c., modified from
337 Christidis 2010) particles. All images are at the same scale.

338

339 **2.2. Electrochemical properties**

340 The different faces of clay particles exhibit different electrochemical properties (Tombacz &
341 Szekeres 2006; Bourg *et al.* 2007; Tournassat *et al.* 2016a). The electrochemical properties of
342 kaolinite particles are mainly controlled by the edge surfaces and the alumina basal surfaces
343 due to the weak negative structural charge on the silica basal surfaces (Tombacz & Szekeres
344 2006) (Fig. 3a). The electrochemical properties of Mt particles and in lesser extent of illite
345 particles are mainly controlled by the basal surfaces due to their larger specific surface area
346 than the edge surfaces and to the structural charge (Tombacz & Szekeres 2004; Leroy & Revil
347 2009; Tournassat *et al.* 2011; Tournassat *et al.* 2013) (Figs 3b and 3c). In the following, we
348 define Q_0 as the surface charge density of the clay mineral (in C m^{-2}), Q_0^b as the basal surface
349 charge density, Q_0^e as the edge surface charge density, Q_i as the negative and permanent
350 structural surface charge density due to isomorphic substitutions, and Q_{EDL} as the surface
351 charge density of the EDL.

352 The quantity Q_0 is an accurate indicator of the EDL properties controlling the IP response
353 because of the electroneutrality condition (Hunter 1981) implying

$$Q_0 + Q_{\mathrm{EDL}} = 0\,, \tag{1}$$

354 and then

$$Q_{\mathrm{EDL}} = -Q_0\,. \tag{2}$$

355 Therefore, according to Eq. 2, a high clay surface charge density magnitude implies a high
356 EDL surface charge density magnitude and potentially a high IP real conductivity response
357 (due to EDL conduction) and a high IP imaginary conductivity response (due to EDL
358 polarisation) (Leroy & Revil 2009). The quantity Q_0 depends on the contributions of the edge
359 and basal surfaces considering

$$Q_0 = \frac{Q_0^e SS_e + Q_0^b SS_b}{SS}\,, \tag{3}$$

360 where SS_e is the edge specific surface area (in $m^2\ g^{-1}$), SS_b is the basal specific surface area,
361 and *SS* is the total specific surface area, $SS = SS_e + SS_b$.

362 The surface charge density Q_0^e is controlled by the amphoteric aluminol, >Al-OH, and silanol,
363 >Si-OH, hydroxyl surface sites that are sensitive to pH and salinity of the surrounding
364 electrolyte due to proton desorption and adsorption on mineral surface (e.g., >S-OH $\leftrightarrow$ >S-
365 O^- + H^+ where >S = >Al or >Si) and salt counter-ion adsorption and desorption in the Stern
366 layer (e.g., >S-O^- + $M^+ \leftrightarrow$ >S-O^- –M^+ where M^+=Na^+) (Leroy & Revil 2004; Tombacz &
367 Szekeres 2004; Tombacz & Szekeres 2006; Tournassat *et al.* 2016a). The alumina basal
368 surface of kaolinite particle is also sensitive to pH and salinity (Tombacz & Szekeres 2006).
369 In absence of strong Q_i influence and dissolution/precipitation reactions, Q_0^e magnitude

should increase when pH moves from the point of zero charge (PZC, pH value where the surface charge involving only amphoteric sites is zero). Indeed, in these conditions, when pH decreases from PZC, mineral edge surface charge should become more positive because of the increasing adsorption of protons H^+, and when pH increases from PZC, mineral edge surface charge should become more negative because of the increasing desorption of protons H^+ (Leroy *et al.* 2011). In these conditions also, $\left|Q_0^e\right|$ should increase when salinity increases because of the adsorption of salt counter-ions in the Stern layer (Leroy *et al.* 2013). The replacement of chemically adsorbed protons by salt cations mostly adsorbed further away from the mineral surface in the Stern layer increases the magnitude of the negative surface charge (the surface charge due to negative oxygen atoms is not compensated by H^+ anymore, see Fig. 5).

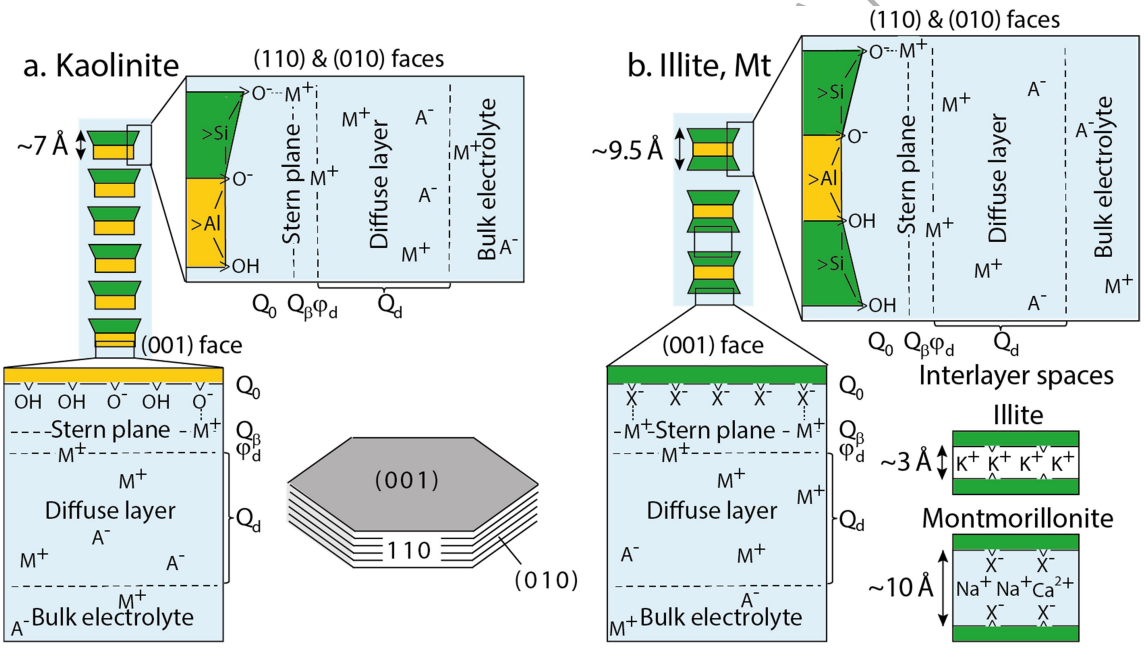

Figure 5. Sketch of the electrochemical properties of (a.) kaolinite, (b.) illite and Mt particles in contact with a 1:1 electrolyte like NaCl or KCl (modified from Leroy & Revil 2009). The electrical potential φ_d is assumed to the located at the *d*-plane delimiting the beginning of the diffuse layer from the mineral surface. In Figure 5b, the white color in the interlayer space means that cations are non-solvated and the blue color in the interlayer space means that cations are fully-solvated.

388

389 Illite and Mt particles exhibit a permanent and negative structural charge on their basal
390 surface (Q_0^b value typically between –0.20 C m^{-2} and –0.10 C m^{-2}) due to isomorphic
391 substitutions within the mineral crystal (Grim 1962; Bourg *et al.* 2007; Leroy *et al.* 2007;
392 Leroy *et al.* 2017b). This structural surface charge is partly compensated by non-solvated
393 cations (e.g., K^+ or NH_4^+ ions with low hydration energy) and hydrated cations (e.g., Na^+
394 and/or Ca^{2+}ions) in the interlayer space of illite and Mt (dioctahedral smectite), respectively
395 (Melkior *et al.* 2009; Tournassat *et al.* 2015). In most of natural Mts, Na^+ and Ca^{2+} ions
396 commonly coexist in the interlayer space (Tournassat *et al.* 2011). Hydrated cations such as
397 Na^+ ions have a significant mobility in the interlayer space of Mt (for instance, around 20% of
398 their mobility in bulk water according to the molecular dynamic simulations of Tournassat *et*
399 *al.* 2009) whereas non-solvated cations such as K^+ ions have a negligible mobility in the
400 interlayer space of illite (Ruiz Pestana *et al.* 2016). Therefore, in the following, we consider
401 that the interlayer space of Mts such as Na-Mt is conductive and polarizable in the mHz to
402 kHz frequency range on the contrary to the illite interlayer space.

403 The behavior of the clay surface charge is therefore more complicated than for oxides such as
404 SiO_2 (Leroy *et al.* 2013) or TiO_2 (Leroy *et al.* 2011) or carbonates (Li *et al.* 2016) because, as
405 written previously, the different faces have not the same electrochemical properties
406 (Tournassat *et al.* 2013). For instance, the PZC of the edge face of Na-Mt is around 6.5
407 whereas its basal faces do not exhibit a PZC value because of the strong influence of the
408 negative structural surface charge (Tombacz & Szekeres 2004). The basal faces (or surfaces)
409 of illite and Mt are less sensitive to pH and salinity than their edge face because the hydroxyl
410 sites are less abundant and of the strong influence of the structural surface charge (Tournassat
411 *et al.* 2015). In a system where protons and hydroxide ions are the only aqueous species, the
412 point of zero net proton charge (PZNPC) of a mineral defines the pH at which the positively

and negatively charged functional groups on its surface are equal (Hao *et al.* 2018). For clay minerals presenting both pH-dependent surface charge and a permanent structural surface charge, the PZNPC is a better indicator of the state of the surface charge than the PZC (Tombacz & Szekeres 2004). The PZNPC of clays decreases to lower pH with increasing, e.g., NaCl concentration in bulk water (not influenced by the electrically charged surface) because of the structural charge influence, which is stronger for, e.g., Na-Mt or illite than for kaolinite (Avena & De Pauli 1998; Tombacz & Szekeres 2006). Tombacz & Szekeres (2006) reported that the PZNPC of Na-Mt ranges from around 8.75 at a salinity of 0.01 M NaCl to around 6.75 at a salinity of 1 M NaCl and that the PZNPC of kaolinite ranges from around 6.75 at a salinity of 0.01 M NaCl to around 5.25 at a salinity of 1 M NaCl (see their Fig. 6). This confirms that the structural charge influence on clay surface charge is stronger for Na-Mt than for kaolinite and hence that the surface charge of kaolinite is more sensitive to pH and salinity compared to the surface charge of Na-Mt. Using measured PZNPC values, Hao *et al.* (2018) showed that the surface charge of kaolinite is more sensitive to pH and salinity compared to the surface charge of Mt and also illite in a lesser extent (a significant part of the structural surface charge of illite is compensated by non-solvated K^+ counter-ions).

The outer mineral surface charge, i.e., the mineral surface charge not compensated by the interlayer counter-ions, is compensated by counter-ions adsorbed in the "compact" Stern layer that has a solid-like water viscosity and is located between the mineral surface and the shear (or slipping) plane when water flow occurs on the mineral surface (Revil & Leroy 2001). The remaining outer mineral surface charge is compensated by counter-ions in excess and co-ions in deficiency compared to their concentration in bulk water that follow a Boltzmann type distribution in the diffuse part of the EDL (Leroy & Revil 2004) (Fig. 5). The high negative surface charge on the basal faces of Mt and illite favors counter-ion condensation within the Stern layer (Leroy & Revil 2009). This is the reason why the fraction of the surface charge

compensated by the Stern layer on the external basal surface of such clay minerals (f_Q) is typically above 50% (Leroy & Revil 2004; Tombacz & Szekeres 2004; Leroy *et al.* 2007; Leroy & Revil 2009; Leroy *et al.* 2015). The f_Q quantity is of paramount importance for SIP models because they consider that the Stern and diffuse layers have different contributions to measured SIP data (e.g., de Lima & Sharma 1992; Leroy & Revil 2009; Revil 2012; Okay *et al.* 2014; Leroy *et al.* 2017b; Qi & Wu 2024). It is defined by:

$$f_Q = \frac{Q_\beta}{Q_\beta + Q_d} = -\frac{Q_\beta}{Q_0}, \tag{4}$$

where Q_β and Q_d are the surface charge densities of the Stern and diffuse layers (in C m^{-2}), respectively. The f_Q quantity can be estimated using ion adsorption experiments and surface complexation models (e.g., basic Stern, triple layer or extended Stern layer models) (e.g., Yates *et al.* 1974; Hiemstra & VanRiemsdijk 1996; Sahai & Sverjensky 1997). In addition, in our knowledge, there is no study on the fraction of the counter-charge controlled by the Stern layer on the edge surfaces of illite and Mt. However, we can expect, in average, lower f_Q values for the edge surfaces than for the external basal surfaces of illite and Mt and higher f_Q values for the edge surfaces of these minerals than for the surfaces of kaolinite because of the structural charge influence on the edge surfaces of illite and Mt. Indeed, Secor & Radke (1985) followed by, e.g., Bourg *et al.* (2007), Tournassat *et al.* (2013), and Tournassat *et al.* (2016a) showed that there is a spill-over effect of the electrostatic potential on the external basal surface onto the electrostatic potential on the edge surface, which can increase the magnitude of the edge negative surface charge in neutral to basic pH conditions and favor Stern layer ion condensation. (Grosse & Delgado 2010)

In water, clay particles in contact with each other form aggregates in particular because of EDL interactions between particles (Fig. 6) (Mc Bride & Baveye 2002). Attractive edge-to-face interactions (when pH < PZC of the edge faces) and repulsive face-to-face interactions as well as edge-to-edge interactions regulate the size and shape of the clay aggregate and its internal porosity, which are strongly depend on pH and salinity (e.g., Leroy *et al.* 2015, Leroy *et al.* 2017b, Rasmusson *et al.* 1997, Sondi *et al.* 1996, Tombacz & Szekeres 2006). The critical coagulation concentration (CCC) is defined as the minimum concentration of salt counter-ions to induce coagulation of colloidal particles. Above the CCC, which is typically between 0.01 and 0.1 mol L^{-1} (M) for dispersed clays in NaCl electrolyte, clay particles coagulate due to diffuse layer compression and form larger particles with more interlayer space for illite and Mt than at lower salinities (e.g., Sondi *et al.* 1996, Rasmusson *et al.* 1997, Tombacz & Szekeres 2004, Tombacz & Szekeres 2006, Leroy *et al.* 2015, Leroy *et al.* 2017b, Mendieta *et al.* 2021).

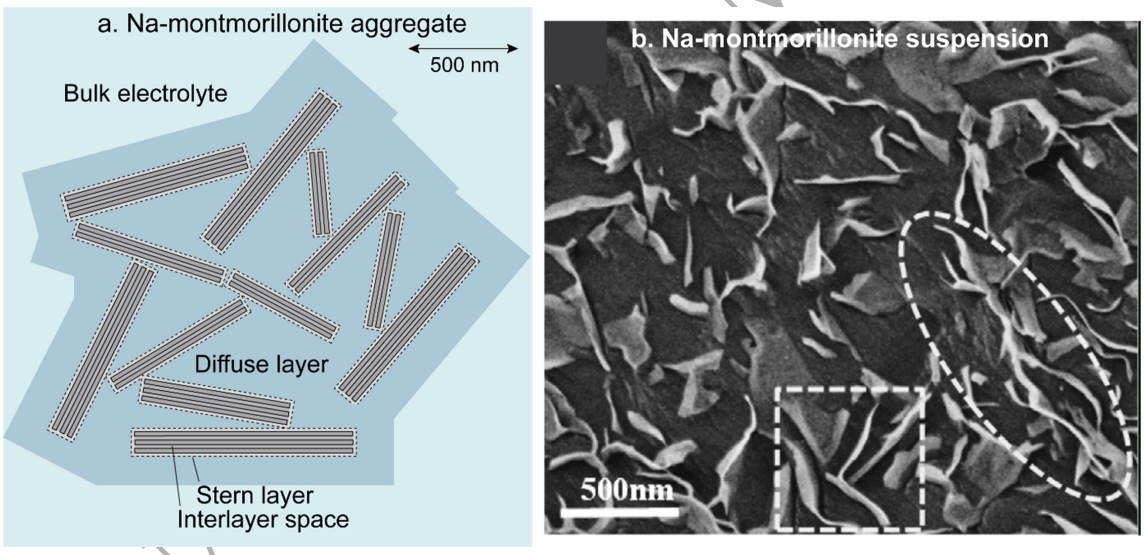

Figure 6. Sketch of a Na-Mt aggregate containing interacting clay particles (a., modified from Leroy *et al.* 2015, in reality particles are thinner than those represented here) and Cryo-SEM images of high-pressure frozen and freeze-fractured SWy-2 bentonite in distilled water with 5% (wt/wt) solid content (b., Na-ion exchanged gel, modified from Mouzon *et al.* 2016).

476 The surface conductivity influencing IP measurements is defined as the excess of electrical
477 conductivity in the EDL compared to in bulk water integrated over the thickness of the EDL
478 (Revil & Glover 1997; Lyklema & Minor 1998). According to O'Konski 1960, surface
479 conductivity contributes to particle conductivity when the thickness (or radius) of the particle
480 is larger than the thickness of the EDL. However, the EDL can be thicker than clay such as
481 illite or Na-Mt particle (section 2.1.), meaning that in that case it can contribute to water
482 conductivity (Dufreche *et al.* 2001; Leroy & Revil 2009). In addition, the electrochemical
483 properties and surface conductivity of kaolinite are more sensitive to pH and salinity than the
484 electrochemical properties and surface conductivity of Mt and illite in a lesser extent (Leroy
485 & Revil 2004). Furthermore, because a kaolinite TO sheet has a weaker structural surface
486 charge and a kaolinite particle has a smaller specific surface area than an illite or a Mt
487 particle, kaolinite has weaker electrochemical and adsorption properties, and hence surface
488 conductivity than illite and Mt (Leroy & Revil 2004; Tombacz & Szekeres 2006; Okay *et al.*
489 2014). Mt surface conductivity should be higher than illite surface conductivity because Mt
490 has a larger reactive specific surface area than illite (Leroy & Revil 2009). This should be
491 particularly true for Na-Mt containing hydrated and mobile Na^+ cations in its interlayer space.
492 This conclusion also means that the laboratory CEC measurement, which depends on the
493 product of the surface charge density (Q_0) with the reactive specific surface area (Leroy *et al.*
494 2007; Okay *et al.* 2014), cannot be used to characterize the electrochemical and IP properties
495 of clays such as kaolinite because of the strong dependence of Q_0 on the bulk pore water
496 composition (pH, salinity). Indeed, CEC laboratory measurements are done using a particular
497 bulk water composition (Khaled & Stucki 1991) that does not correspond necessarily to the
498 bulk pore water composition in the laboratory samples during SIP measurements and in-situ
499 during field geophysical measurements. However, the laboratory CEC measurement could be
500 safely employed to characterize the electrochemical and IP properties of Mt and in a lesser

extent of illite and soils, sediments and rocks containing a significant fraction of these minerals because of the strong influence of the permanent and negative structural charge (Vinegar & Waxman 1984; Revil 2012; Weller *et al.* 2013; Okay *et al.* 2014; Leroy *et al.* 2017b).

3 THE PETROPHYSICAL SIP MODEL

After presenting the microstructural and electrochemical properties of kaolinite, illite, and Mt clays, we explain here the petrophysical SIP model. During SIP measurement, a sinusoidal electrical current in the mHz to kHz frequency range is injected into the clay material and the resulting voltage is recorded in order to measure the complex conductivity of the clay material. In this section, we briefly explain the SIP model developed by Leroy *et al.* (2017b) for dilute Mt suspensions. We then explain the extension of this SIP model to clay materials containing significant content of kaolinite, illite or Mt considering interlayer space conduction and polarisation for Na-Mt and Maxwell-Wagner polarisation.

Our conductivity model is based on Ampere's law, one of the four Maxwell's equations. This law considers that the magnetic field strength is influenced by conduction current satisfying Ohm's law and displacement current due to the time-varying electrical field (Maxwell 1892), that is

$$\nabla \times \mathbf{H} = \mathbf{J}_C + \mathbf{J}_D , \tag{5}$$

where $\mathbf{H}$ is the magnetic field strength (in A m^{-1}), and $\mathbf{J}_C$ is the electrical current density due to conduction current (in A m^{-2}) and $\mathbf{J}_D$ is the electrical current density due to displacement current, which are defined by

$$\mathbf{J}_C = \sigma \mathbf{E}, \tag{6}$$

522 and

$$\mathbf{J}_D = \frac{\partial \mathbf{D}}{\partial t}, \tag{7}$$

523 where σ is the electrical conductivity of the investigated medium (in S m^{-1}), **E** is the applied
524 electrical field (in V m^{-1}), **D** is the dielectric displacement (in C m^{-2}), and t is the time (in s).
525 The applied sinusoidal electrical field and the dielectric displacement are respectively defined
526 by

$$\mathbf{E} = \mathbf{E}_0 \exp(i\omega t), \tag{8}$$

527 and

$$\mathbf{D} = \varepsilon \mathbf{E}, \tag{9}$$

528 where i is the imaginary number ($i^2 = -1$), ω is the angular frequency of the applied electrical
529 current (in rad s^{-1}; $\omega = 2\pi f$ with f being the frequency in Hz), and ε is the permittivity of the
530 investigated medium (in F m^{-1}). By using Eqs 6 to 9, we finally obtain for the total current
531 density

$$\mathbf{J}_t = (\sigma + i\omega\varepsilon)\mathbf{E}, \tag{10}$$

532 and then for the medium conductivity

$$\sigma^* = \sigma + i\omega\varepsilon. \tag{11}$$

533

534

535

536 **3.1. Model assumptions**

537 A clay aggregate can be decomposed into different compartments: bulk (electroneutral) water,
538 diffuse layer water, Stern layers and interlayer spaces of particles, which exhibit different
539 electrical conductivities (Leroy & Revil 2009; Okay *et al.* 2014; Leroy *et al.* 2017b) (Fig. 6).
540 Following the works of Revil and co-workers (e.g., Leroy & Revil 2009; Jougnot *et al.* 2010a;
541 Revil 2012; Okay *et al.* 2014), the SIP model of Leroy *et al.* (2017b) assumes that the bulk
542 water and the diffuse layer water surrounding clay particles are continuous at the scale of the
543 laboratory centimetric measurement and hence do not contribute to the polarisation of the
544 particles. According to Leroy *et al.* (2017b), the bulk and diffuse layer waters only contribute
545 to conductivity at zero frequency (direct current, DC conductivity) influencing clay material
546 in-phase conductivity (real component of clay material complex conductivity). Similarly to
547 the SIP models of Revil and co-workers, the model of Leroy *et al.* (2017b) considers that the
548 Stern layers around clay particles are discontinuous at the scale of the centimetric laboratory
549 measurement and polarize, influencing clay material in-phase conductivity and quadrature
550 conductivity (imaginary component of clay material complex conductivity). Leroy *et al.*
551 2017b) assumed that the clay material polarizes at the scale of the clay aggregate, meaning
552 that they considered the polarisation of the Stern layers on the clay particles in contact with
553 each other. Similarly to the works of Revil and co-workers, Leroy *et al.* (2017b) did not
554 consider the adsorption/desorption kinetics of the ions in the Stern layer as well as their
555 exchange with the ions in the diffuse layer and bulk water because they assumed that these
556 processes are instantaneous compared to the movements of the ions in the EDL and bulk
557 water.

558 Following the works of, e.g., Dufreche *et al.* (2001), Bourg *et al.* (2003), Rotenberg *et al.*
559 (2005), and Cadene *et al.* (2006), we consider that some fully hydrated ions (such as Na^+ ions

and/or Ca^{2+} ions in a lesser extent (Tournassat *et al.* 2009; Bourg & Sposito 2011; Greathouse *et al.* 2016)) are mobile in the interlayer space of Mt particle and hence contribute to low-frequency conduction and polarisation in clay particles in contact with each other.

Our model has been developed to extract porosity, electrical formation factor, clay aggregate size distribution, and water and surface conductivities from complex conductivity measurements. It was used to interpret SIP measurements reported in Mendieta *et al.* (2021) from the measured experimental conditions (Maineult *et al.* 2024). For instance, prior to the SIP measurements, Mendieta *et al.* (2021) measured the mass of the dry clay powder, i.e. the solid mass (δ_s) (in g), before mixing it with a NaCl electrolyte of known salt concentration (C^0_{NaCl}) (in mol L^{-1}, M). It should be noted that the SIP model presented here can be generalized to any type of electrolyte but the case of a NaCl electrolyte is considered here in order to compare in Maineult *et al.* (2024) the model to the experimental data reported in Mendieta *et al.* 2021 on kaolinite, illite and Mt muds. In these experiments, the (total) volume of the sample (V_t) (in m^3), the temperature (T_C) (in °C) ($T_C = T - 273.15$ where T is the absolute temperature in K), and the (total) masses of the sample before and after water evaporation (δ_t^0 and δ_t^{l}, respectively) (in g), were also recorded. In our model, measured δ_s and V_t values as well as the measured volume fraction of the main clay mineral in the solid phase (ξ_c) (by X-ray diffraction, XRD) are used to compute the volumes of the different components of the clay material intervening in the SIP model (Appendix A). Measured T_C values are used to compute the model parameter values as a function of temperature (Appendix B), and measured C^0_{NaCl}, δ_t^0 and δ_t^{l} values are used to calculate NaCl concentration in bulk water after evaporation and bulk water chemical composition (Appendix C). Na^+ and Cl^- ion mobilities in bulk water intervening in the SIP model are also computed as a function of NaCl concentration (Appendix B) because of the mutual influence

584 of cations and anions decreasing their mobility and hence the related electrical conductivity
585 (Leroy *et al.* 2015).

586

587 **3.2. Calculation of the EDL properties**

588 We have developed here a new approach to directly compute the electrical potential at the *d*-
589 plane (delimiting the beginning of the diffuse layer from the mineral surface) (φ_d) (in V, Fig.
590 4), from the fraction of the counter-charge in the Stern layer (f_Q) and the mineral surface
591 charge density (Q_0) (in C m^{-2}). The mineral surface charge density is computed from ratio of
592 the measured cation exchange capacity (CEC) (in meq g^{-1}) to the specific surface area where
593 cation exchange reactions occur on clay mineral surface (*SS*) (in m^2 g^{-1}) (Okay *et al.* 2014).
594 The *SS* quantity can be estimated using crystallography (Leroy & Revil 2004). In the case of
595 Na-Mt, it can be approximated by the total specific surface area of the basal surfaces (SS_b)
596 (Leroy *et al.* 2015; Leroy *et al.* 2017b). Clay particles exhibit different electrical potentials on
597 their surfaces (Bourg *et al.* 2007; Tournassat *et al.* 2013). Our approach considers a
598 dominating electrical potential at the *d*-plane on the clay surface (φ_d) and not a distribution of
599 φ_d potentials on the clay surface, which will make the modeling considerably more complex.
600 The advantage of our approach is also that it does not need an electrostatic surface
601 complexation model, that can be very complicated, to estimate φ_d from bulk water chemical
602 composition (see for example Tournassat *et al.* 2013).

603 The φ_d potential is a physical quantity of paramount importance in the colloidal and interface
604 science and geophysical communities focusing on understanding electrochemical properties.
605 Indeed, it regulates electrostatic attraction/repulsion on charged surfaces and electrostatic
606 interaction between charged surfaces when in contact with a polar solvent like water (Gouy

1910; Chapman 1913; Grahame 1947). This electrical potential is commonly assumed to be equal to the zeta potential inferred from electrokinetic measurements when a shear or slipping plane involving polar solvent flow occurs on the surfaces (von Smoluchowski 1905; von Smoluchowski 1921). Knowing the φ_d potential value is useful here to compute two processes considered in the SIP model: (i) the effect of the diffuse layer on Stern layer polarisation through the M parameter value ($M \geq 1$) and (ii) the electrical conductivity of the diffuse layer (that will be fully explained in Sections 3.3 and 3.4). According to Lyklema *et al.* (1983), ions in the diffuse layer counterbalance locally ions in the polarized Stern layer to ensure local electroneutrality. This effect decreases the length of the pathway of the migrating ions in the Stern layer and hence it decreases the relaxation time of the polarized Stern layer (Fig. 1, Fig. 7b and Eq. 15).

Ions in the diffuse layer counteracting ions in the Stern layer contributing to polarisation could in principle not contribute also to conduction via electromigration. However, on the contrary to what is shown by Lyklema *et al.* (1983) about the EDL of a single particle, the diffuse layers around clay particles are probably connected and may fill a significant part of the pore space in clay materials when the clay concentration in the sample is large. For instance, clay muds can contain a large mass of dry clay powder per liter of sample. In the SIP experiments of Mendieta *et al.* (2021), clay muds contain about one thousand grams of dry clay powder per liter of sample. This means that the diffuse layers are not necessarily disconnected and hence solely counteracting Stern layer polarisation. For this reason, we consider in the following that the diffuse layer contributes to DC conductivity implying that $M = 1$ theoretically (no effect of diffuse layer on Stern layer polarisation). However, we also consider here a hybrid approach assuming that the diffuse layer can locally (at the particle scale) counter-balance Stern layer polarisation through the computation of $M \geq 1$ and contribute also to conduction via electromigration (at the sample scale).

The following function is minimized to estimate φ_d from f_Q and Q_0 (Appendix D) (knowing the bulk water chemical composition):

$$\left| \sqrt{2\overline{\varepsilon_w} k_B T 10^3 N_A \sum_{i=1}^{N} C_i^b \left[\exp\left(-\frac{q_i \varphi_d}{k_B T} \right) - 1 \right]} - Q_0 \left(1 - f_Q \right) \right| = 0 , \quad (12)$$

where $\overline{\varepsilon_w}$ represents the mean water permittivity (in F m^{-1}) including in the interlayer space of Na-Mt (we consider that ε_w has the same value in the diffuse layer and bulk water, see Appendix B for ε_w values), and k_B is the Boltzmann's constant (~1.381×10^{-23} J K^{-1}). In Eq. 12, N represents the number of different ion species i in bulk water with ion concentration C_i^b (in mol L^{-1}, M) and charge $q_i = \pm e z_i$ (in C) where "+" and "–" stand for cations and anions, respectively, e is the elementary (or electron) charge (~1.602×10^{-19} C), z_i is the ion valence (e.g., $z_i = 1$ for sodium or chloride ion and $z_i = 2$ for calcium, magnesium or sulfate ion), and N_A is the Avogadro's number (~6.022×10^{23} mol^{-1}).

In the case of Na-Mt, we assume in Eq. 12 the same electrical potential φ_d in the interlayer space and diffuse layer on the external clay surface (Dufreche *et al.* 2001). However, for Na-Mt, the water permittivity value intervening in the calculation of φ_d (Eqs 12 or 15) and of the differential capacitance of the diffuse layer C_d (in F m^{-2}) (Hunter 1981) to compute M (Eq. 16) could be significantly smaller in the interlayer space than in the diffuse layer on the external clay surface due to the stronger electrical field (Hiemstra & Van Riemsdijk 2006) and the weaker level of hydration (Wander & Clark 2008) in the interlayer space. In our knowledge, the water permittivity value is not accurately known in the interlayer space of Na-Mt and should be between clay solid permittivity value ($\varepsilon_s \cong 5\varepsilon_0$ where ε_0 is vacuum permittivity, see Section 3.3) and bulk water permittivity value ($\varepsilon_w \cong 78.3\varepsilon_0$ for distilled

water at a temperature of 298.15 K, see Appendix B). For that reason, we consider in the following that the water permittivity value in the interlayer space of Na-Mt is half the value in bulk water, i.e. $\varepsilon_{in} = \varepsilon_w / 2$. In Eqs 12 or 15 and 16, water permittivity is therefore computed using

$$\overline{\varepsilon_w} = \frac{\varepsilon_w V_w^d + \varepsilon_{in} V_{in}}{V_w^d + V_{in}} = \frac{\varepsilon_w}{V_w^d + V_{in}} \left(V_w^d + \frac{V_{in}}{2} \right), \tag{13}$$

where V_w^d is the calculated diffuse layer volume (in m^3) and V_{in} is the calculated interlayer space volume when it contains mobile ions such as Na^+ ions (see Appendix A).

If Q_0 is considered homogeneous on the mineral surface, it can be computed as a function of the measured CEC and *SS* (Okay *et al.* 2014) using

$$Q_0 = -\frac{eN_A \, \mathrm{CEC}}{10^3 \, SS}, \tag{14}$$

then when using Eq. 14, Eq. 12 becomes

$$\left| \sqrt{2\overline{\varepsilon_w} k_B T 10^3 N_A \sum_{i=1}^{N} C_i^b \left[\exp\left(-\frac{q_i \varphi_d}{k_B T} \right) - 1 \right]} - \frac{eN_A \, \mathrm{CEC}}{10^3 \, SS} \left(1 - f_Q \right) \right| = 0 . \tag{15}$$

The *M* parameter value (Lyklema *et al.* 1983) is computed from f_Q and φ_d according to

$$M = 1 + \frac{qQ_\beta}{k_B T C_d}, \tag{16}$$

where q is the mean charge of the counter-ions in the Stern layer (in C; $q = \pm ez$ with z is the mean valence of the counter-ions). The Q_β quantity in Eq. 16 is determined as a function of f_Q and the surface charge density on the mineral surface (Q_0) using (Appendix D)

$$Q_\beta = -f_Q Q_0 , \tag{17}$$

where Q_0 can be computed as a function of the measured CEC and *SS* using Eq. 7. The differential capacitance of the diffuse layer (Eq. 16) is determined from φ_d (Leroy *et al.* 2017a) according to

$$C_d = -\frac{\partial Q_d}{\partial \varphi_d} = \sqrt{\frac{\overline{\varepsilon_w}}{2k_B T}} \frac{10^3 N_A \sum_{i=1}^{N} q_i C_i^b \exp\left(-\frac{q_i \varphi_d}{k_B T}\right)}{\sqrt{10^3 N_A \sum_{i=1}^{N} C_i^b \left[\exp\left(-\frac{q_i \varphi_d}{k_B T}\right) - 1\right]}}, \tag{18}$$

and for a symmetric electrolyte of valence *z*, Eq. 18 reduces to

$$C_d = \overline{\varepsilon_w} \kappa \cosh\left(\frac{ze\varphi_d}{2k_B T}\right), \tag{19}$$

where $\kappa = \chi_D^{-1}$ is the inverse of the Debye length (in m^{-1}) (see Eq. A5 (Lyklema *et al.* 1983)), and then the *M* parameter value is computed from f_Q and Q_0 or CEC and *SS* according to Eqs 12 to 18 or 19. The case $M = 1$ corresponds to the Schwarz's model (Schwarz 1962) with no effect of the diffuse layer on Stern layer polarisation. Leroy *et al.* (2017b) found that $M \cong 4$ for the basal surface of Na-Mt, meaning that, in this case, ions in the diffuse layer significantly decrease the length of the pathways and then the relaxation time of ions in the polarized Stern layer according to the generalized Schwarz model of Lyklema *et al.* (1983).

3.3. Aggregate conductivity due to surface conductivity

A mineral surface in contact with a polar solvent like water and submitted to a low-frequency electrical field expresses a surface conductivity response due to migrating ions in the EDL (O'Konski 1960). Surface conductivity (or surface conductance) is defined as a surface

quantity in Siemens and not as a volume quantity in Siemens per meter. However, we will define it in the following as a volume quantity because of its widespread use as a volume quantity like water conductivity in the geophysical community. Like our water conductivity model, our "surface" conductivity model is based on Ampere's law (Eq. 5) (e.g., Schwarz 1962; de Lima & Sharma 1992; Chelidze & Gueguen 1999; Leroy *et al.* 2008). The resulting surface conductivity is written as (Eq. 11)

$$\sigma_s^*(\omega) = \sigma_s(\omega) + i\omega\varepsilon_s, \tag{20}$$

where the first term (a complex quantity when considering EDL polarisation) arises from conduction current and the second term arises from displacement current in the presence of an applied sinusoidal electrical field with ε_s being the solid dielectric constant (in F m^{-1}). In our model, we assume that clay aggregates control the surface conductivity and induced polarisation response of the material. Therefore, the symbol σ_s^* reported in Eq. 20 for the clay aggregate conductivity corresponds to the symbol used by most IP practitioners for the surface conductivity of the whole material. In addition, in Eq. 20, we do not consider anisotropy in the calculation of the surface conductivity. Therefore, our model is particularly adapted to unconsolidated clay materials like uncompacted clay muds.

Clay particles assemble themselves to make clay aggregate, which can be considered a spherical object with a surface area made of the surface area of the particles constituting the aggregate at first approximation. Leroy *et al.* (2017b) developed petrophysical relationships to compute σ_s in Eq. 20 from the Mt aggregate microstructural and electrochemical properties. They considered that the surface conductivity of a Mt aggregate is similar to the surface conductivity of an equivalent spherical particle with an amplified surface area S (in m^2) compared to its surface area if it is considered perfectly smooth and non-porous. In the model of Leroy *et al.* (2017b), S is related to the specific surface area of all the polarising clay

platelets inside the aggregate (Fig. 6a). In addition, the SIP model of Leroy *et al.* (2017b) uses the generalized Schwarz model developed by Lyklema *et al.* (1983) to simulate the effect of the diffuse layer on the polarisation of the Stern layer surrounding clay particle (Fig. 1a).

It is actually very difficult and time-consuming to numerically compute the induced polarisation response of interacting clay particles because of (i) their high aspect ratio, (ii) heterogeneities in their surface electrical properties, and (iii) the physical-chemical mechanisms involved in the interaction (interacting diffuse and Stern layers) (Tournassat *et al.* 2013; Tournassat *et al.* 2015; Bücker *et al.* 2019). For this reason, we have to make the assumption that the polarisation of the Stern layers surrounding interacting clay particles is equivalent to the polarisation of a porous clay aggregate with an effective diameter surrounded by a Stern layer (for more information read Leroy et al. 2017b). In other words, in our model, the Stern layers of the interacting clay particles are assumed continuous at the scale of the aggregate (see also discussion in Jougnot et al. 2010a).

It should be noted that, according to some molecular dynamic (MD) simulations, most Na^+ and Ca^{2+} counter-ions in the Stern layer on the Mt basal surface may be adsorbed beyond the first hydration layer plane as outer-sphere surface complexes, keeping their hydration shell (e.g., Tournassat *et al.* 2009; Bourg & Sposito 2011). These MD simulations show that these counter-ions may behave in terms of ion diffusivity like ions in the diffuse layer. Therefore, according to these MD simulations, we can expect that, for a single clay particle, Stern layer polarisation is not necessarily different from diffuse layer polarisation on the basal surface of Mt.

We can attribute diffuse layer polarisation to a volume diffusion mechanism involving migrating ions in the diffuse layer and ions clouds in bulk water (Fig. 1b) and Stern layer polarisation to a surface diffusion mechanism associated with migrating ions on particle

surface (Fig. 1a) (Grosse & Delgado 2010). Delgado *et al.* (1998) showed that the contribution of the volume diffusion mechanism to the measured dielectric dispersion of polymer latex particles in the kHz to MHz frequency range decreases compared to the contribution of the surface diffusion mechanism because the space available for volume diffusion in bulk water decreases faster than the space available for surface diffusion when the particle concentration in solution increases (here particle volume fraction ranges from 3 to 16%). Concentrated colloidal suspensions like clay muds have solid volume fractions typically above 10% (Richter & Sevick-Muraca 2000). Our model is adapted to saturated clay materials presenting typically a high concentration of clay particles with a high fraction of counter-charge in the Stern layer (f_Q). For this reason, we believe that the polarisation models of Schwarz (1962) and Lyklema *et al.* (1983) considering surface diffusion is suitable to simulate EDL polarisation of clay materials.

According to Leroy *et al.* (2017b), the low-frequency surface conductivity of clay aggregates is written as

$$\sigma_s^* = \frac{2}{3}\phi_a \beta_S f_Q Q_V \sum_{k=1}^{L} f(d_k) \frac{i\omega\tau_k}{1+i\omega\tau_k} + i\omega\alpha\rho_s\varepsilon_0, \quad (21)$$

where ϕ_a is the porosity of the aggregate (dimensionless, between 0 and 1), β_S is the mean ion mobility of the counter-ions moving along the particle surface contributing to low-frequency polarisation (in $m^2\ s^{-1}\ V^{-1}$), and Q_V is the excess of counter-charge of the EDL per unit pore volume of the aggregate (in C m^{-3}). In Eq. 21, $f(d_k)$, $k = 1 \ldots L$, is the discretized distribution of the effective sizes of the aggregates with d_k being the effective diameter of the k^{th} aggregate (in m) and L being the number of different effective diameters of the aggregates in the model. In Eq. 21 also, τ_k is the relaxation time of the polarized Stern layers within the k^{th} aggregate (in s), $\alpha = 0.00191$ $m^3\ kg^{-1}$ is an empirical value that was used by Olhoeft

750 (1981) to adjust solid permittivity spectra, ρ_s is the solid volumetric mass density (in kg m^{-3}),
751 and $\varepsilon_0 \cong 8.854\times10^{-12}$ F m^{-1} is the vacuum permittivity. According to the crystallographic unit
752 cell, $\rho_s \cong 2700$ kg m^{-3} for clays (~2600, 2700, and 2800 kg m^{-3} for kaolinite, smectite and
753 illite, respectively (Leroy & Revil 2009); ~2710 and 2840 kg m^{-3} for Kunipia-G Na-Mt
754 (Massat *et al.* 2016) and MX80 bentonite – mostly made of Na-Mt (Tournassat & Appelo
755 2011)). Using $\varepsilon_s \cong \alpha\rho_s\varepsilon_0$ (Eqs 20 and 21), the $\varepsilon_s \cong 4.57\varepsilon_0$ value obtained accordingly is close
756 to the $\varepsilon_s \cong 5.5\varepsilon_0$ value reported by Robinson (2004) for Mt using time domain reflectometry.

757 Determining ρ_s by crystallography, i.e. dividing the mass of the solid by the estimated related
758 volume, is a challenging task for clays because of the difficulty to accurately measure the
759 effective thickness of a clay layer *t*. Tournassat *et al.* (2016b) used molecular dynamic
760 simulations to estimate *t*. They found ρ_s = 2930 ± 100 kg m^{-3} for swelling clays such as Mt,
761 which is significantly higher than the Mt ρ_s value estimated by pycnometry, ~2700 kg m^{-3}
762 that can be representative of the volumetric mass density value of the solid part of a non-
763 swelling clay such as illite (value down to 2600 kg m^{-3}).

764 In our model ϕ_a (Eq. 21) is not necessarily the sample porosity ϕ because we assume that
765 some types of clay aggregates like illite and Mt aggregates contain only diffuse layer and
766 interlayer space waters (case of Na-Mt) and the sample can also contain bulk water. The word
767 "sample" is referred here to the investigated porous medium at the scale of the representative
768 elementary volume (REV) where the measured electrical properties are considered
769 homogeneous (Revil & Leroy 2004).

770 Aggregate porosity ϕ_a is calculated from the computed volumes of the different components
771 of the aggregate:

$$\phi_a = \frac{V_S + V_w^d + V_w^b}{V_{sc} + V_S + V_w^d + V_w^b}, \quad (22)$$

for kaolinite, and

$$\phi_a = \frac{V_S + V_w^d}{V_{sc} + V_{in} + V_S + V_w^d}, \quad (23)$$

for illite, and

$$\phi_a = \frac{V_{in} + V_S + V_w^d}{V_{sc} + V_{in} + V_S + V_w^d}, \quad (24)$$

for Mt such as Na-Mt, where V_w^b, V_S, and V_{sc} are the computed volumes of the bulk water (in m^3), Stern layer, and solid clay layers, respectively (Appendix A). Kaolinite aggregates are assumed to contain bulk and diffuse layer waters (Eq. 22). Illite and Mt aggregates are assumed to contain only diffuse layer and interlayer space waters (case of Na-Mt) because of their higher specific surface areas and surface charges and smaller pores than kaolinite aggregates (Leroy & Revil 2009; Okay *et al.* 2014; Leroy *et al.* 2015) (Eqs 23 and 24). In Eq. 23, we assume that K^+ ions migrate and diffuse very slowly along the surface of the interlayer space of illite compared to in bulk water (Ruiz Pestana *et al.* 2016) and hence that they do not contribute to low-frequency polarisation. We also assume that they do not contribute to low-frequency conduction. In Eq. 24, we assume that Na^+ ions migrate and diffuse significantly along the surface of the interlayer space of Na-Mt compared to in bulk water (Bourg *et al.* 2003; Zhang *et al.* 2014) and hence that they contribute to low-frequency polarisation (Rotenberg *et al.* 2005; Cadene *et al.* 2006). We also assume that the part of Na^+ ions in the interlayer space not contributing to low-frequency polarisation contributes to low-frequency conduction. Mt particles containing immobile or very slow ions in the interlayer space can be considered similar to illite particles.

Sample porosity can be computed using

$$\phi = \frac{V_{in} + V_w^d + V_w^b}{V_t}, \tag{25}$$

where V_t is the measured total volume of the sample during laboratory SIP measurements.

In Eq. 21, the Q_V quantity is given by

$$Q_V = \rho_s \left(\frac{1-\phi_a}{\phi_a} \right) e N_{\mathrm{A}} \, \mathrm{CEC} \, . \tag{26}$$

Eq. 21 uses a parallel mixing formula for the modelling of the surface conductivity (σ_s) of the clay aggregates with different sizes, i.e., to compute σ_s, the surface conductivity response of each aggregate of diameter d_k is weighted by its volume relative to the total volume of the aggregates (Lesmes & Morgan 2001). As stated by, e.g., Lesmes & Morgan (2001), the parallel mixing formula gives an upper bound for the computed complex surface conductivity of different sized particles. The geometric mean mixing formula, which arises from random networks consisting of both parallel and serial connections (Madden 1976), would have been more realistic to compute σ_s in our model because it gives an average value for the computed complex surface conductivity of different sized particles. However, the parameter optimization procedure to obtain the relaxation time distribution intervening in the SIP model from the SIP measurement is the Debye decomposition approach here (for more details on the optimization procedure, see Maineult *et al.* 2024). The parallel mixing formula gives for σ_s an Eq. equivalent to the Eq. inferred from the Debye decomposition approach (Lesmes & Morgan 2001). This is the reason why our model uses the parallel mixing formula for σ_s similarly to Lesmes & Morgan (2001).

The relaxation time τ_k (Eq. 21) is the time necessary for the counter-ions in the Stern layers within the k^{th} aggregate to diffuse back to their equilibrium position once the Stern layers are polarized due to ion electromigration (Lyklema *et al.* 1983; de Lima & Sharma 1992; Chelidze & Gueguen 1999) (see Fig. 1a). It is related to the effective diameter and surface ion mobility using

$$\tau_k = \frac{{d_k}^2 |q|}{8 k_B T \beta_S M}, \tag{27}$$

Eq. 27 shows that, for each aggregate of effective size d_k, the generalized Schwarz model of Lyklema *et al.* (1983) considers one relaxation time τ_k (see Fig. 7). Therefore, our model simulates a Debye type response for the increase of the real and imaginary conductivity response due to the low-frequency polarisation of the aggregate. Our modelling approach is based on (i) fitting the complex conductivity spectra to obtain the relaxation time distribution $f(\tau_k), k = 1 \ldots L$ and the aggregate size distribution $f(d_k), k = 1 \ldots L$ (for more details on the optimization procedure see Leroy *et al.* 2017b and Maineult *et al.* 2024) and (ii) computing the aggregate effective size d_k from the obtained relaxation time τ_k and the optimized β_S value obtained by successfully comparing measured to predicted complex conductivity spectra using

$$d_k = \sqrt{8 \frac{k_B T}{|q|} \beta_S M \tau_k}, \tag{28}$$

meaning that for given values of β_S and τ_k, increasing M increases the calculated effective diameter of the k^{th} aggregate.

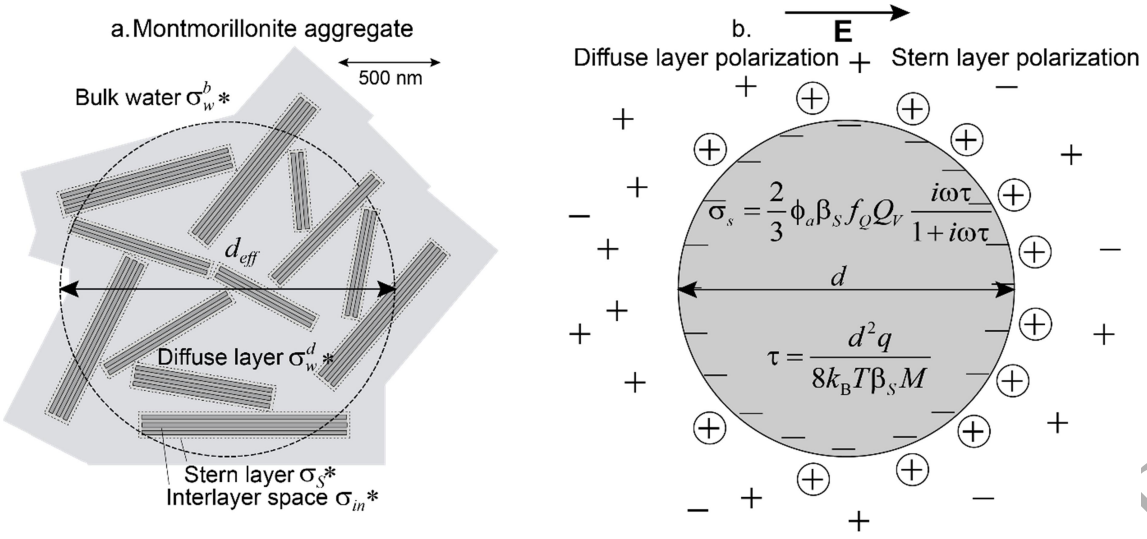

826

827 **Fig. 7.** Sketch of a Mt aggregate with an effective diameter d_{eff} showing the clay particles
828 interacting with each other and the electrical conductivities of the different components (not
829 in scale) (a.). Sketch of the equivalent Stern layer polarisation model of Leroy *et al.* (2017b)
830 around a negatively charged spherical particle in contact with a monovalent electrolyte (not in
831 scale) (b.) (modified from Leroy *et al.* 2017b).

832 In Section 3.4, we will explain that the diffuse layer of clay particles, especially illite and Na-
833 Mt particles, contributes to the volume conductivity of the clay material and not to its surface
834 conductivity because the diffuse layer thickness can be larger than the clay particle thickness
835 (see Section 2.1) (O'Konski 1960; Dufreche *et al.* 2001). However, at high ionic strength I
836 (typically ≥ 1 M), the diffuse layer is highly compressed. For instance, the Debye length
837 characterizing the diffuse layer thickness is ~3 Å at T = 298.15 K and ionic strength I = 1 M
838 (see Eqs A5 and B16). In that case, the diffuse layer thickness can be smaller than the
839 thickness of the clay layer and the assumption of the diffuse layer contributing to the volume
840 conductivity of the clay material does not necessarily hold because the diffuse layer can
841 contribute to the surface conductivity of the particle (O'Konski 1960). For larger clay particles
842 such as kaolinite particles, the diffuse layer can be thinner than the particle thickness for
843 smaller ionic strengths compared to illite and Mt particles and hence contribute to surface
844 conductivity according to O'Konski (1960). For this reason, in this condition, Eq. 21 becomes
845 (Leroy *et al.* 2008; Leroy *et al.* 2017b) (Appendix D):

$$\sigma_s^* = \frac{2}{3}\phi_a \sum_{k=1}^{N_{d_k}} f(d_k)\left[\beta_S f_Q \frac{i\omega\tau_k}{1+i\omega\tau_k} + \widetilde{B_d}\left(1-f_Q\right)\right]Q_V + i\omega\alpha\rho_s\varepsilon_0, \quad (29)$$

where $\widetilde{B_d}$ is the ion mobility in the diffuse layer including electro-osmosis (in m^2 s^{-1} V^{-1}) (Revil & Glover 1997), which can be calculated according to

$$\widetilde{B_d} = \frac{1}{\vartheta}\left(\beta_i^b + \frac{2\overline{\varepsilon_w}k_B T}{\eta_w |q_i|}\right), \quad (30)$$

where ϑ ($\vartheta \geq 1$) is a weighting coefficient that can be considered equal to the ratio of the surface area of the clay particles within the clay aggregate to the surface area of the equivalent non-porous spherical particle (Appendix D), β_i^b is the ion mobility in the diffuse layer due to electro-migration (in m^2 s^{-1} V^{-1}) (we assume $\beta_i^d = \beta_i^b$) and q_i is the charge of the dominating ion in the diffuse layer (in C). For a 1:1 electrolyte such as NaCl electrolyte at a temperature of 298.15 K, the second term of Eq. 30 describing electro-osmotic effect yields $m_i^d \cong 3.78\times10^{-8}$ m^2 s^{-1} V^{-1} using $\overline{\varepsilon_w} = 78.3\varepsilon_0$, which is in the same order of magnitude than the ion mobility values in bulk and distilled water due to electro-migration ($\beta_{Na^+}^b = 5.17\times10^{-8}$ m^2 s^{-1} V^{-1} and $\beta_{Cl^-}^b = 7.89\times10^{-8}$ m^2 s^{-1} V^{-1}), meaning that electro-osmosis cannot be neglected for the computation of the surface conductivity of the diffuse layer. It should be noted that it may be complicated to distinguish between Stern and diffuse layer contributions to surface conductivity especially at high ionic strengths due to diffuse layer compression and to the fact that most counter-ions adsorbed in the Stern layer on the basal clay surface may be adsorbed as outer-sphere surface complexes.

3.4. Water conductivity

We consider that the bulk water and the diffuse layer water are continuous at the scale of the SIP laboratory measurement and hence that they only contribute to the in-phase conductivity of the clay material (see Section 3.1). The self-consistent model developed by Hashin & Shtrikman (1962) is used here to compute clay water conductivity including the diffuse layer contribution in the case of the thick diffuse layer assumption. It is written as

$$\sigma_w^* = \sigma_w^{b*}\left[1+\frac{3\Theta_w^d\left(\sigma_w^{d*}-\sigma_w^{b*}\right)}{3\sigma_w^{b*}+\left(1-\Theta_w^d\right)\left(\sigma_w^{d*}-\sigma_w^{b*}\right)}\right], \tag{31}$$

where σ_w^{b*} is the bulk water conductivity (in S m^{-1}) (including displacement current), σ_w^{d*} is the diffuse layer water conductivity (including displacement current), and Θ_w^d is the volume fraction of diffuse layer water over diffuse layer and bulk waters. Hashin & Shtrikman (1962) presented two models as the upper and lower bounds to calculate the effective property that depends on which one of the two components is seen as the matrix or as the inclusion. In Eq. 31 the bulk water is the matrix and the diffuse layer water is the inclusion during the calculation. This equation is the lower bound obtained by Hashin & Shtrikman (1962). Eq. 31 has been developed under the condition $\left|\sigma_w^{d*}\right| > \left|\sigma_w^{b*}\right|$ that is usually satisfied because there is an excess of mobile counter-ions in the diffuse layer compared to in bulk water to compensate the surface charge not compensated by counter-ions in the Stern layer (Bourg & Sposito 2011). In our model, the Θ_w^d quantity in Eq. 31 is determined from the computed volumes of the different components of the aggregate (Appendix A). It is given by

$$\Theta_w^d = \frac{V_w^d}{V_w^b + V_w^d}, \tag{32}$$

for kaolinite and illite, and

$$\Theta_w^d = \frac{V_w^d + V_{in}}{V_w^b + V_w^d + V_{in}}, \tag{33}$$

for Mt such as Na-Mt, where the interlayer space of Na-Mt is considered contributing of the volume conductivity of the clay material similarly to the diffuse layer. Despite the fact that the thickness of the interlayer space of Na-Mt is on the same order of magnitude than the thickness of a TOT layer (~ 1 nm), we do not consider here that the part of the interlayer space of Na-Mt that is not polarizing contributes to the surface conductivity of Na-Mt. Indeed, it would be too complicated to consider at this stage of our model that the interlayer space would contribute to the surface conductivity of the clay particles while the diffuse layer would contribute to the water conductivity. In addition, our diffuse layer surface conductivity model is more accurate for low φ_d potentials (see Appendix D) whereas our diffuse layer volume conductivity model is adapted to any φ_d potentials when the electrolyte is symmetric (Leroy *et al.* 2015) (see discussion related to Eq. 38).

In Eq. 31, the conductivity of the bulk water is calculated from ion concentration in bulk water (C_i^b) considering conduction current from ion electro-migration and displacement current (Leroy *et al.* 2008)

$$\sigma_w^b* = e10^3 N_A \sum_{i=1}^{N} z_i \beta_i^b C_i^b + i\omega\varepsilon_w. \tag{34}$$

In our model, simulated bulk water conductivity depends on temperature and salinity. Indeed, in Eq. 34, computed ion mobilities in bulk water (β_i^b) consider temperature and salinity (here NaCl concentration) effects, and bulk water permittivity (ε_w) considers temperature effect (Appendix B). Computed ion concentration in bulk water (C_i^b) also considers temperature effect via the simulation of the temperature dependence of the dissociation constant of water

molecules K_w (Eq. B2). For other types of ions than Na^+ and Cl^- ions (here H^+, OH^-, and Ca^{2+} and SO_4^{2-} ions), $\beta_i^b(298)$ is also computed as a function of the measured ion self-diffusion coefficient in distilled water at a temperature of 298.15 K $\overline{D_i^b}(298)$ (in $m^2\ s^{-1}$) reported in the phreeqc.dat database of the geochemical software PhreeqC (Parkhurst & Appelo 2013).

Similarly to bulk water conductivity, the volume conductivity of the diffuse layer water is determined from

$$\sigma_w^d* = \frac{e10^3 N_A}{\chi_d}\int_{x=0}^{x=\chi_d}\sum_{i=1}^{N} z_i B_i^d(x) C_i^b \exp\left[-\frac{q_i\varphi(x)}{k_B T}\right]dx + i\omega\overline{\varepsilon_w}, \quad (35)$$

$$B_i^d(x) = \beta_i^b \pm \beta_{eo}^d(x), \quad (36)$$

$$\beta_{eo}^d(x) = \frac{\varepsilon_w}{\eta_w}\left[\varphi(x) - \varphi_d\right], \quad (37)$$

$$\varphi(x) = \frac{4k_B T}{ez}\tanh^{-1}\left[\tanh\left(\frac{ez\varphi_d}{4k_B T}\right)\exp(-\kappa x)\right], \quad (38)$$

where x is the distance from the beginning of the diffuse layer on the mineral side (in m), $\chi_d = 2\chi_D$ (Leroy *et al.* 2015) is the diffuse layer thickness (with χ_D being the Debye length, Eq. A5) (in m), B_i^d is the ion mobility in the diffuse layer considering electro-osmosis (in $m^2\ s^{-1}\ V^{-1}$), and $\kappa = \chi_D^{-1}$ (Leroy *et al.* 2015; Leroy *et al.* 2017b). Liquid water dynamic viscosity η_w (in $Pa\ s^{-1}$) intervening in the calculation of the effect of electro-osmosis on surface conductivity (Eqs 36 and 37) is calculated as a function of temperature (Appendix B). In Eq. 36, "+" and "–" stand for cations and anions, respectively. Eqs 35-38 show interesting features for the conductivity calculations compared to the surface conductivity model based

on Bikerman's equation (Eqs D12-D14). Eq. 36 shows that electro-osmosis associated with cations increases conductivity whereas it shows that electro-osmosis associated with anions decreases conductivity because the solvent flow due to the excess of cationic charge is in the direction of the electrical field and the solvent flow due to the excess of anionic charge is in the direction opposed to the electrical field (Leroy *et al.* 2015). Eqs 37-38 also show that electro-osmotic effect on conductivity is larger when the φ_d potential is larger hence when ionic strength decreases at fixed pH or when pH is further away from IEP (pH value where the zeta potential is zero) at fixed ionic strength. Bikerman's Eq. considers that both cations and anions increase conductivity due to electro-osmosis with a value independent on the φ_d potential (Eqs D12 to D14).

When the electrolyte is not symmetric, the following equation, based on the Debye-Hückel approximation (Appendix D), is used to calculate the electrical potential distribution in the diffuse layer instead of Eq. 38:

$$\varphi(x) = \varphi_d \exp(-\kappa x). \tag{39}$$

Leroy *et al.* (2017b) computed the diffuse layer volume conductivity by calculating an average (or mean) electrical potential in the diffuse layer φ_m (see Appendix E). In that case, Eqs 35-38 become

$$\sigma_w^d * = e10^3 N_A \sum_{i=1}^{N} z_i B_i^d C_i^b \exp\left(-\frac{q_i \varphi_m}{k_B T}\right) + i\omega\overline{\varepsilon_w}, \tag{40}$$

$$B_i^d = \beta_i^b \pm \beta_{eo}^d, \tag{41}$$

$$\beta_{eo}^d = \frac{\varepsilon_w}{\eta_w}\left(\varphi_m - \varphi_d\right), \tag{42}$$

933 where φ_m is computed according to Eq. E8 for kaolinite and illite and Eq. E7 for Mt with
934 mobile ions in the interlayer space such as Na-Mt. Compared to Eqs 35-38, Eqs 40-42 and E8
935 or E7 have the advantage of not needing to know the electrical potential distribution in the
936 diffuse layer. But, these Eqs can be more approximate because they do not consider the
937 dependence on the distance from the beginning of the diffuse layer, which can lead to less
938 accurate results for the electrical potential distribution, especially at high ionic strengths when
939 the diffuse layer is highly compressed.

940

941 **3.5. Clay material conductivity**

942 In our model, minerals other than the main clay mineral are not considered conductive
943 compared to water and the main clay mineral. The effect of weakly conductive minerals on
944 the modeled background conductivity (σ_0*), which does not consider surface conductivity of
945 the particles, is considered here using the self-consistent model developed by Hashin &
946 Shtrikman (1962)

$$\sigma_0^* = \sigma_w^* \left[1 - \frac{3(1-c)}{(3-c)} \right], \tag{43}$$

947 where

$$c = \frac{V_w^d + V_w^b}{V_{so} + V_S + V_w^d + V_w^b} \tag{44}$$

948 for kaolinite, and

$$c = \frac{V_w^d + V_w^b}{V_{so} + V_{in} + V_S + V_w^d + V_w^b} \tag{45}$$

949 for illite, and

$$c = \frac{V_{in} + V_w^d + V_w^b}{V_{so} + V_{in} + V_S + V_w^d + V_w^b}, \quad (46)$$

for Mt such as Na-Mt, where c is the volume fraction of conductive water and V_{so} (in m^3) is the volume of weakly conductive minerals (compared to water and the main clay mineral; the subscript "*so*" means "solid other") that are not considered conductive. The Stern layer is considered not conductive too here.

The differential effective medium (DEM) theory (Bruggeman 1935; Hanai 1968; Sen 1984) is used to compute the complex conductivity of the clay material after calculating the complex conductivity of the clay particles and of the background medium. In the DEM theory, clay particles are embedded in a self-similar way in the background medium (Sen *et al.* 1981). First, a particle is added to the background medium and the influence of the particle upon the conductivity of the medium is calculated. Then, the particle/background medium mixture is added to another particle in the background medium and the conductivity of the new particle/background medium mixture is calculated, and so on following an iterative procedure until the desired porosity is reached (see Fig. 1 of Sen *et al.* 1981). The DEM theory assumes that the current crosses all the pores in the investigated sample, i.e. that they are all interconnected electrically speaking. It works well to describe the electrical properties (conductivity and permittivity) of porous media with small and isolated contact regions between the particles. It also simulates Maxwell-Wagner polarisation effect (Leroy & Revil 2009).

The DEM model uses the computed background conductivity (σ_0*), aggregate surface conductivity (σ_s*) and volume fraction of the solid part of the main clay mineral in the investigated sample ($\Omega_s = V_{sc} / V_t$) (V_{sc} in m^3 is the volume of the solid part of the main clay mineral and V_t in m^3 is the sample volume, see Appendix A) to compute clay material

complex conductivity. The cementation exponent m characterizing the shape of the aggregates should also be considered in the DEM model. For a sphere, $m = 1.5$ (Sen *et al.* 1981), and the m value increases when the aspect ratio (width to height ratio) of the particles or grains of the material with a σ_s^* conductivity increases. For unconsolidated sands packed in the laboratory, $m = 1.3$, consolidated sandstones, $1.8 \le m \le 2$, and $1.2 \le m \le 4$ for most minerals with goethite and clay particles exhibiting the highest m values (Mendelson & Cohen 1982).

In our model, DEM computations are presented as follows. The initial electrical conductivity of the clay material is the background conductivity, i.e. $\sigma^* = \sigma_0^*$ initially. Inclusions are clay aggregates with a given shape that have a surface conductivity σ_s^* and volume fraction $d\Omega_s$ and that are randomly oriented in the medium. The depolarisation factor of inclusions, L ($0 \le L \le 1$), which is necessary for the calculation of σ^* according to the DEM theory (Mendelson & Cohen 1982), is calculated from

$$L = \frac{3 + \sqrt{9 + 36m^2 - 60m}}{6m}, \tag{47}$$

and, finally, clay material conductivity is calculated iteratively using

$$d\sigma^* = \frac{\sigma^*}{3} \frac{\left(\sigma_s^* - \sigma_0^*\right)\left[\left(1+3L\right)\sigma_s^* + \left(5-3L\right)\sigma_0^*\right]}{\left[L\sigma_s^* + \left(1-L\right)\sigma_0^*\right]\left[\left(1-L\right)\sigma_s^* + \left(1+L\right)\sigma_0^*\right]} \frac{d\Omega_s}{1-\Omega_s}, \tag{48}$$

$$\sigma^* = \sigma^* + d\sigma^*, \tag{49}$$

$$\Omega_s = \Omega_s + d\Omega_s, \tag{50}$$

where $\Omega_s = 0$ (and $\sigma^* = \sigma_0^*$) initially and $d\Omega_s = V_{sc} / \left(V_t N_s\right)$ with N_s being the number of solid inclusions to reach the volume fraction of the solid part of the main mineral in the sample. Compared to the integrated form of the DEM model, the iterative form shown here

gives more accurate complex conductivity predictions when the inclusion eccentricity increases compared to spherical inclusions (Sen *et al.* 1981; Mendelson & Cohen 1982; Sen 1984).

Our model allows determining the effective diameter of the k^{th} clay aggregate, d_k (Eq. 28). The following equation (Mendelson & Cohen 1982) can be solved numerically to determine aggregate eccentricity (e_c) from the depolarisation factor (L) calculation

$$\left| L - \frac{1+e_c^{\,2}}{e_c^{\,3}}\left(e_c - \tan^{-1} e_c\right)\right| = 0\,, \tag{51}$$

and the height of the k^{th} aggregate is then given by

$$h_k = \sqrt{\frac{d_k^{\,2}}{1+e_c^{\,2}}}\,. \tag{52}$$

4 CONCLUSIONS

We have developed a new mechanistic model to understand and predict laboratory and field spectral induced polarisation (SIP) measurements on clay materials including kaolinite, illite and montmorillonite minerals from their microstructural and electrochemical properties. Water and surface conductivities, electrical formation factor, cementation exponent, sample porosity, and clay aggregate effective size distribution can be extracted from the comparison of the model to experimental data.

Our model simulates the complex conductivity (for frequencies typically from 1 mHz to tens of kHz) of the different components of the clay material. It considers the polarisation of the Stern layers around clay particles forming aggregates and contributing to surface conductivity as well as montmorillonite interlayer space conduction and polarisation and Maxwell-Wagner

polarisation. The diffuse layer is assumed to contribute to the water conductivity or to the surface conductivity of the particle depending notably if the diffuse layer is thicker or not to the clay particle. Our model assumes one main clay mineral contributing to conduction and polarisation in the low-frequency range. It also uses parameter values that can be measured in the laboratory independently to the SIP measurements like temperature (for temperatures between 2 and 87°C where water is liquid), cation exchange capacity (CEC), clay powder mass, initial salinity, and sample volume. The parameters to be adjusted are the fraction of the counter-charge and the ion effective mobility in the Stern layer, the number of stacked solid layers per particle for montmorillonite and the cementation exponent characterizing the shape of the aggregates.

The comparison of the model predictions to the experimental data including the optimization procedure and the related discussion will be presented in a companion paper. Our model can test the validity of some petrophysical models developed at larger scale that are commonly used to interpret laboratory and field SIP measurements. In addition, its predictions can be checked by purely numerical SIP models developed at the scale of the clay particle and constrained by high-resolution characterization measurements.

ACKNOWLEDGMENTS

This study was carried out within the framework of the ANR EXCITING and IMAGE projects (grants ANR-17-CE06-0012 and ANR-21-CE04-0013, respectively, funded by the French National Research Agency). Philippe Leroy warmly thanks Francis Claret for his support and Christophe Tournassat for the fruitful discussions. The work of Philippe Leroy was also supported by the EURAD work package DONUT (EC grant agreement No. 847593).

We thank the editor, Léa Levy, and the two reviewers, Viacheslav Emelianov and Youzheng Qi, for providing thorough and constructive reviews of our manuscript.

DATA AVAILABILITY STATEMENT

No data were used for this theoretical paper.

REFERENCES

Aizebeokhai, A. P. & Oyeyemi, K. D., 2014. The use of the multiple-gradient array for geoelectrical resistivity and induced polarization imaging, *Journal of Applied Geophysics,* **111,** 364-376, doi:10.1016/j.jappgeo.2014.10.023.

Ali, E. S., Askalany, A. A., Harby, K., Diab, M. R., Hussein, B. R. M. & Alsaman, A. S., 2021. Experimental adsorption water desalination system utilizing activated clay for low grade heat source applications, *Journal of Energy Storage,* **43,** 103219, doi:10.1016/j.est.2021.103219.

Avena, M. J. & De Pauli, C. P., 1998. Proton adsorption and electrokinetics of an Argentinean montmorillonite, *Journal of Colloid and Interface Science,* **202,** 195-204, doi:10.1006/jcis.1998.5402.

Azua-Bustos, A., Fairén, A. G., Silva, C. G., Carrizo, D., Fernández-Martínez, M. Á., Arenas-Fajardo, C., Fernández-Sampedro, M., Gil-Lozano, C., Sánchez-García, L., Ascaso, C., Wierzchos, J. & Rampe, E. B., 2020. Inhabited subsurface wet smectites in the hyperarid core of the Atacama Desert as an analog for the search for life on Mars, *Sci Rep,* **10**, doi:10.1038/s41598-020-76302-z.

Bandura, A. V. & Lvov, S. N., 2006. The Ionization Constant of Water over Wide Ranges of Temperature and Density, *Journal of Physical and Chemical Reference Data,* **35,** 15-30, doi:10.1063/1.1928231.

Bernard, O., Kunz, W., Turq, P. & Blum, L., 1992. Self-Diffusion in Electrolyte-Solutions Using the Mean Spherical Approximation, *Journal of Physical Chemistry,* **96,** 398-403, doi:10.1021/J100180a074.

Bikerman, J. J., 1940. Electrokinetic equations and surface conductance. A survey of the diffuse double layer theory of colloidal solutions *Transactions of the Faraday Society,* **35,** 154-160, doi:10.1039/TF9403500154.

Binley, A., Hubbard, S. S., Huisman, J. A., Revil, A., Robinson, D. A., Singha, K. & Slater, L. D., 2015. The emergence of hydrogeophysics for improved understanding of subsurface processes over multiple scales, *Water Resources Research,* **51,** 3837-3866, doi: 10.1002/2015WR017016.

Binley, A. & Kemna, A., 2005. DC resistivity and induced polarization methods. *in Hydrogeophysics*, pp. 129-156, ed. Hubbard, Y. R. a. S. S. Springer, New York,

Binley, A. & Slater, L., 2020. *Resistivity and Induced Polarization: Theory and Applications to the Near-Surface Earth,* edn, Vol., Cambridge University Press, doi:10.1017/9781108685955.

Bø Hunvik, K. W., Loch, P., Wallacher, D., Kirch, A., Cavalcanti, L. P., Rieß, M., Daab, M., Josvanger, V., Grätz, S., Yokaichiya, F., Knudsen, K. D., Rodrigues Miranda, C., Breu, J. & Fossum, J. O., 2021. CO2 Adsorption Enhanced by Tuning the Layer

Charge in a Clay Mineral, *Langmuir,* **37,** 14491-14499, doi:10.1021/acs.langmuir.1c02467.
Bourg, I. C., Bourg, A. C. M. & Sposito, G., 2003. Modeling diffusion and adsorption in compacted bentonite: a critical review, *Journal of Contaminant Hydrology,* **61,** 293-302, doi:10.1016/s0169-7722(02)00128-6.
Bourg, I. C. & Sposito, G., 2011. Molecular dynamics simulations of the electrical double layer on smectite surfaces contacting concentrated mixed electrolyte (NaCl-CaCl2) solutions, *Journal of Colloid and Interface Science,* **360,** 701-715, doi:10.1016/j.jcis.2011.04.063.
Bourg, I. C., Sposito, G. & Bourg, A. C. M., 2007. Modeling the acid-base surface chemistry of montmorillonite, *Journal of Colloid and Interface Science,* **312,** 297-310, doi:10.1016/j.jcis.2007.03.062.
Brigatti, M., Galán, E. & Theng, B., 2013. 2 Chapter 2 - Structure and Mineralogy of Clay Minerals *in Handbook of Clay Science*, pp. 21-81, ed. Bergaya, F. L., G. Elsevier, Oxford,
Bristow, T. F., Rampe, E. B., Achilles, C. N., Blake, D. F., Chipera, S. J., Craig, P., Crisp, J. A., Des Marais, D. J., Downs, R. T., Gellert, R., Grotzinger, J. P., Gupta, S., Hazen, R. M., Horgan, B., Hogancamp, J. V., Mangold, N., Mahaffy, P. R., McAdam, A. C., Ming, D. W., Morookian, J. M., Morris, R. V., Morrison, S. M., Treiman, A. H., Vaniman, D. T., Vasavada, A. R. & Yen, A. S., 2018. Clay mineral diversity and abundance in sedimentary rocks of Gale crater, Mars, *Science Advances,* **4,** eaar3330, doi:10.1126/sciadv.aar3330.
Bruggeman, D. A. G., 1935. Berechnung verschiedener physikalischer Konstanten von heterogenen Substanzen, *Annalen der Physik,* **416,** 636-664, doi:10.1002/andp.19354160705.
Bücker, M., Flores Orozco, A., Undorf, S. & Kemna, A., 2019. On the Role of Stern- and Diffuse-Layer Polarization Mechanisms in Porous Media, *Journal of Geophysical Research: Solid Earth,* **124,** 5656-5677, doi:10.1029/2019jb017679.
Busch, A., Bertier, P., Gensterblum, Y., Rother, G., Spiers, C. J., Zhang, M. & Wentinck, H. M., 2016. On sorption and swelling of CO2 in clays, *Geomechanics and Geophysics for Geo-Energy and Geo-Resources,* **2,** 111-130, doi:10.1007/s40948-016-0024-4.
Cadene, A., Rotenberg, B., Durand-Vidal, S., Badot, J. C. & Turq, P., 2006. Dielectric spectroscopy as a probe for dynamic properties of compacted smectites, *Physics and Chemistry of the Earth,* **31,** 505-510, doi:10.1016/j.pce.2006.04.002.
Chapman, D. L., 1913. A contribution to the theory of electrocapillarity *Philosophical Magazine Serie 6,* **25,** 475-481, doi: 10.1080/14786440408634187.
Charlet, L., Alt-Epping, P., Wersin, P. & Gilbert, B., 2017. Diffusive transport and reaction in clay rocks: A storage (nuclear waste, CO2, H2), energy (shale gas) and water quality issue, *Advances in Water Resources,* **106,** 39-59, doi:10.1016/j.advwatres.2017.03.019.
Chelidze, T. L. & Gueguen, Y., 1999. Electrical spectroscopy of porous rocks: a review - I. Theoretical models, *Geophysical Journal International,* **137,** 1-15, doi:10.1046/j.1365-246x.1999.00799.x.
Christidis, G. E., 2010. Industrial Clays**,** 341-414, doi:10.1180/EMU-notes.9.9.
de Lima, O. A. L. & Sharma, M. M., 1992. A generalized Maxwell-Wagner theory for membrane polarization in shaly sands, *Geophysics,* **57,** 431-440, doi:10.1190/1.1443257.
Delgado, A. V., Arroyo, F. J., Gonzalez-Caballero, F., Shilov, V. N. & Borkovskaya, Y. B., 1998. The effect of the concentration of dispersed particles on the mechanisms of low-frequency dielectric dispersion (LFDD) in colloidal suspensions, *Colloids and*

Surfaces a-Physicochemical and Engineering Aspects, **140,** 139-149, doi:10.1016/S0927-7757(97)00272-0.
Dufreche, J. F., Marry, V., Bernard, O. & Turq, P., 2001. Models for electrokinetic phenomena in montmorillonite, *Colloids and Surfaces a-Physicochemical and Engineering Aspects,* **195,** 171-180, doi:10.1016/S0927-7757(01)00840-8.
El Alam, J., Revil, A. & Dick, P., 2023. Influence of the water content on the complex conductivity of bentonite, *Engineering Geology,* **322**, doi:10.1016/j.enggeo.2023.107183.
Fixman, M., 1980. Charged Macromolecules in External Fields. I. The Sphere, *Journal of Chemical Physics,* **72,** 5177-5186, doi:10.1063/1.439753.
Gehin, A., Greneche, J. M., Tournassat, C., Brendle, J., Rancourt, D. G. & Charlet, L., 2007. Reversible surface-sorption-induced electron-transfer oxidation of Fe(II) at reactive sites on a synthetic clay mineral, *Geochimica Et Cosmochimica Acta,* **71,** 863-876, doi:10.1016/j.gca.2006.10.019.
Glaser, D. R., Barrowes, B. E., Shubitidze, F. & Slater, L. D., 2023. Laboratory investigation of high-frequency electromagnetic induction measurements for macro-scale relaxation signatures, *Geophysical Journal International,* **235,** 1274-1291, doi:10.1093/gji/ggad298.
Gouy, G., 1910. Sur la constitution de la charge électrique à la surface d'un électrolyte, *Annales de Physique (Paris) Série 4,* **9,** 457-468, doi: 10.1051/jphystap:019100090045700.
Grahame, D. C., 1947. The Electrical Double Layer and the Theory of Electrocapillarity, *Chemical Reviews,* **41,** 441–501, doi:10.1021/cr60130a002.
Greathouse, J. A., Cygan, R. T., Fredrich, J. T. & Jerauld, G. R., 2016. Molecular Dynamics Simulation of Diffusion and Electrical Conductivity in Montmorillonite Interlayers, *The Journal of Physical Chemistry C,* **120,** 1640-1649, doi:10.1021/acs.jpcc.5b10851.
Grim, R. E., 1962. *Applied Clay Mineralogy,* edn, Vol., McGraw–Hill, New York,
Grosse, C. & Delgado, A. V., 2010. Dielectric dispersion in aqueous colloidal systems, *Current Opinion in Colloid & Interface Science,* **15,** 145-159, doi:10.1016/j.cocis.2009.11.004.
Guggenheim, S. & Martin, R. T., 1995. Definition of Clay and Clay Mineral: Joint Report of the AIPEA Nomenclature and CMS Nomenclature Committees, *Clays and Clay Minerals,* **43,** 255-256, doi:10.1346/ccmn.1995.0430213.
Guisseau, D., Mas, P. P., Beaufort, D., Girard, J. P., Inoue, A., Sanjuan, B., Petit, S., Lens, A. & Genter, A., 2007. Significance of the depth-related transition montmorillonite-beidellite in the Bouillante geothermal field (Guadeloupe, Lesser Antilles), *American Mineralogist,* **92,** 1800-1813, doi:10.2138/am.2007.2398.
Hanai, T., 1968. 5 Electrical properties of emulsions. *in Emulsions Science*, pp. 354-477, ed. Sherman, P. Academic Press, New York,
Hao, W., Flynn, S. L., Alessi, D. S. & Konhauser, K. O., 2018. Change of the point of zero net proton charge (pHPZNPC) of clay minerals with ionic strength, *Chemical Geology,* **493,** 458-467, doi:10.1016/j.chemgeo.2018.06.023.
Hashin, Z. & Shtrikman, S., 1962. A Variational Approach to the Theory of the Effective Magnetic Permeability of Multiphase Materials, *Journal of Applied Physics,* **33,** 3125-3131, doi:10.1063/1.1728579.
Hassan, M. S., Villieras, F., Gaboriaud, F. & Razafitianamaharavo, A., 2006. AFM and low-pressure argon adsorption analysis of geometrical properties of phyllosilicates, *Journal of Colloid and Interface Science,* **296,** 614-623, doi:10.1016/j.jcis.2005.09.028.

Hiemstra, T. & Van Riemsdijk, W. H., 2006. On the relationship between charge distribution, surface hydration, and the structure of the interface of metal hydroxides, *Journal of Colloid and Interface Science,* **301,** 1-18, doi:10.1016/j.jcis.2006.05.008.

Hiemstra, T. & VanRiemsdijk, W. H., 1996. A surface structural approach to ion adsorption: The charge distribution (CD) model, *Journal of Colloid and Interface Science,* **179,** 488-508, doi:10.1006/jcis.1996.0242.

Hunter, R. J., 1981. *Zeta Potential in Colloid Science: Principles and Applications,* edn, Vol., Academic Press, New York, doi: 10.1016/C2013-0-07389-6

Ismadji, S., Soetaredjo, F. E. & Ayucitra, A., 2015. *Clay Materials for Environmental Remediation,* edn, Vol. 25, Springer, Surabaya, doi:10.1007/978-3-319-16712-1.

Jougnot, D., Ghorbani, A., Revil, A., Leroy, P. & Cosenza, P., 2010a. Spectral induced polarization of partially saturated clay-rocks: a mechanistic approach, *Geophysical Journal International,* **180,** 210-224, doi:10.1111/j.1365-246X.2009.04426.x.

Jougnot, D., Revil, A. & Leroy, P., 2009. Diffusion of ionic tracers in the Callovo-Oxfordian clay-rock using the Donnan equilibrium model and the formation factor, *Geochimica Et Cosmochimica Acta,* **73,** 2712-2726, doi:10.1016/j.gca.2009.01.035.

Jougnot, D., Revil, A., Lu, N. & Wayllace, A., 2010b. Transport properties of the Callovo-Oxfordian clay rock under partially saturated conditions, *Water Resources Research,* **46**, doi:10.1029/2009wr008552.

Karaborni, S., Smit, B., Heidug, W., Urai, J. & van Oort, E., 1996. The Swelling of Clays: Molecular Simulations of the Hydration of Montmorillonite, *Science,* **271,** 1102-1104, doi:10.1126/science.271.5252.1102.

Kausar, A., Iqbal, M., Javed, A., Aftab, K., Nazli, Z.-i.-H., Bhatti, H. N. & Nouren, S., 2018. Dyes adsorption using clay and modified clay: A review, *Journal of Molecular Liquids,* **256,** 395-407, doi:10.1016/j.molliq.2018.02.034.

Kemna, A., Binley, A., Cassiani, G., Niederleithinger, E., Revil, A., Slater, L., Williams, K. H., Orozco, A. F., Haegel, F. H., Hordt, A., Kruschwitz, S., Leroux, V., Titov, K. & Zimmermann, E., 2012. An overview of the spectral induced polarization method for near-surface applications, *Near Surface Geophysics,* **10,** 453-468, doi: 10.3997/1873-0604.2012027.

Khaldoun, A., Moller, P., Fall, A., Wegdam, G., De Leeuw, B., Méheust, Y., Otto Fossum, J. & Bonn, D., 2009. Quick Clay and Landslides of Clayey Soils, *Physical Review Letters,* **103**, doi:10.1103/PhysRevLett.103.188301.

Khaled, E. M. & Stucki, J. W., 1991. Iron Oxidation State Effects on Cation Fixation in Smectites, *Soil Science Society of America Journal,* **55,** 550, doi:10.2136/sssaj1991.03615995005500020045x.

Leroy, P., Devau, N., Revil, A. & Bizi, M., 2013. Influence of surface conductivity on the apparent zeta potential of amorphous silica nanoparticles, *Journal of Colloid and Interface Science,* **410,** 81-93, doi:10.1016/j.jcis.2013.08.012.

Leroy, P., Lassin, A., Azaroual, M. & Andre, L., 2010. Predicting the surface tension of aqueous 1:1 electrolyte solutions at high salinity, *Geochimica Et Cosmochimica Acta,* **74,** 5427-5442, doi:10.1016/j.gca.2010.06.012.

Leroy, P., Li, S., Jougnot, D., Revil, A. & Wu, Y., 2017a. Modeling the evolution of complex conductivity during calcite precipitation on glass beads, *Geophysical Journal International,* **209,** 123–140, doi:10.1093/gji/ggx001.

Leroy, P. & Revil, A., 2004. A triple-layer model of the surface electrochemical properties of clay minerals, *Journal of Colloid and Interface Science,* **270,** 371-380, doi:10.1016/j.jcis.2003.08.007.

Leroy, P. & Revil, A., 2009. A mechanistic model for the spectral induced polarization of clay materials, *Journal of Geophysical Research-Solid Earth,* **114,** 1-21, doi:10.1029/2008jb006114.

Leroy, P., Revil, A., Altmann, S. & Tournassat, C., 2007. Modeling the composition of the pore water in a clay-rock geological formation (Callovo-Oxfordian, France), *Geochimica Et Cosmochimica Acta,* **71,** 1087-1097, doi:10.1016/j.gca.2006.11.009.

Leroy, P., Revil, A., Kemna, A., Cosenza, P. & Ghorbani, A., 2008. Complex conductivity of water-saturated packs of glass beads, *Journal of Colloid and Interface Science,* **321,** 103-117, doi:10.1016/j.jcis.2007.12.031.

Leroy, P., Tournassat, C., Bernard, O., Devau, N. & Azaroual, M., 2015. The electrophoretic mobility of montmorillonite. Zeta potential and surface conductivity effects, *Journal of Colloid and Interface Science,* **451,** 21-39, doi:10.1016/j.jcis.2015.03.047.

Leroy, P., Tournassat, C. & Bizi, M., 2011. Influence of surface conductivity on the apparent zeta potential of TiO2 nanoparticles, *Journal of Colloid and Interface Science,* **356,** 442-453, doi:10.1016/j.jcis.2011.01.016.

Leroy, P., Weigand, M., Mériguet, G., Zimmermann, E., Tournassat, C., Fagerlund, F., Kemna, A. & Huisman, J. A., 2017b. Spectral induced polarization of Na-montmorillonite dispersions, *Journal of Colloid and Interface Science,* **505,** 1093-1110, doi:10.1016/j.jcis.2017.06.071.

Lesmes, D. P. & Morgan, F. D., 2001. Dielectric spectroscopy of sedimentary rocks, *Journal of Geophysical Research-Solid Earth,* **106,** 13329-13346, doi:10.1029/2000jb900402.

Li, S., Leroy, P., Heberling, F., Devau, N., Jougnot, D. & Chiaberge, C., 2016. Influence of surface conductivity on the apparent zeta potential of calcite, *Journal of Colloid and Interface Science,* **468,** 262-275, doi:10.1016/j.jcis.2016.01.075.

Li, Z., Dong, M., Li, S. & Huang, S., 2006. CO2 sequestration in depleted oil and gas reservoirs—caprock characterization and storage capacity, *Energy Conversion and Management,* **47,** 1372-1382, doi:10.1016/j.enconman.2005.08.023.

Lide, D. R., 1990. *CRC Handbook of Chemistry and Physics* edn, Vol., CRC Press, Boca Raton,

Liu, J., Wang, S., Javadpour, F., Feng, Q. & Cha, L., 2022. Hydrogen Diffusion in Clay Slit: Implications for the Geological Storage, *Energy & Fuels,* **36,** 7651-7660, doi:10.1021/acs.energyfuels.2c01189.

Lyklema, J., Dukhin, S. S. & Shilov, V. N., 1983. The relaxation of the double-layer around colloidal particles and the low-frequency dielectric-dispersion. Part I. Theoretical Considerations, *Journal of Electroanalytical Chemistry,* **143,** 1-21, doi:10.1016/S0022-0728(83)80251-4.

Lyklema, J. & Minor, M., 1998. On surface conduction and its role in electrokinetics, *Colloids and Surfaces a-Physicochemical and Engineering Aspects,* **140,** 33-41, doi:10.1016/S0927-7757(97)00266-5.

Madden, T. R., 1976. Random Networks and Mixing Laws, *Geophysics,* **41,** 1104-1125, doi:10.1190/1.2035907.

Maineult, A., Leroy, P., Mendieta, A. & Jougnot, D., 2024. A mechanistic model for the complex conductivity of clay materials. II. Comparison to experimental data, *submitted to Geophysical Journal International*.

Malusis, M. A., Shackelford, C. D. & Olsen, H. W., 2003. Flow and transport through clay membrane barriers, *Engineering Geology,* **70,** 235-248, doi:10.1016/s0013-7952(03)00092-9.

Marshall, D. J. & Madden, T. R., 1959. Induced Polarization, a Study of Its Causes, *Geophysics,* **24,** 790-816, doi:10.1190/1.1438659.

Martin, T., Günther, T., Orozco, A. F. & Dahlin, T., 2020. Evaluation of spectral induced polarization field measurements in time and frequency domain, *Journal of Applied Geophysics,* **180**, doi:10.1016/j.jappgeo.2020.104141.

Massat, L., Cuisinier, O., Bihannic, I., Claret, F., Pelletier, M., Masrouri, F. & Gaboreau, S., 2016. Swelling pressure development and inter-aggregate porosity evolution upon hydration of a compacted swelling clay, *Applied Clay Science,* **124-125,** 197-210, doi:10.1016/j.clay.2016.01.002.

Maxwell, J. C., 1892. *A Treatise on Electricity and Magnetism,* third edition edn, Vol., Oxford University Press, London,

Mc Bride, E. F., 2012. Petrology of the Eureka Quartzite (Middle and Late Ordovician), Utah and Nevada, U.S.A, *Rocky Mountain Geology,* **47,** 81-111, doi:10.2113/gsrocky.47.2.81.

Mc Bride, M. B. & Baveye, P., 2002. Diffuse double-layer models, long-range forces, and ordering in clay colloids, *Soil Science Society of America Journal,* **66,** 1207-1217, doi:10.2136/sssaj2002.1207.

Melkior, T., Gaucher, E. C., Brouard, C., Yahiaoui, S., Thoby, D., Clinard, C., Ferrage, E., Guyonnet, D., Tournassat, C. & Coelho, D., 2009. Na+ and HTO diffusion in compacted bentonite: Effect of surface chemistry and related texture, *Journal of Hydrology,* **370,** 9-20, doi:10.1016/j.jhydrol.2009.02.035.

Mendelson, K. S. & Cohen, M. H., 1982. The effect of grain anisotropy on the electrical-properties of sedimentary-rocks, *Geophysics,* **47,** 257-263, doi:10.1190/1.1441332.

Mendieta, A., Jougnot, D., Leroy, P. & Maineult, A., 2021. Spectral Induced Polarization Characterization of Non-Consolidated Clays for Varying Salinities—An Experimental Study, *Journal of Geophysical Research: Solid Earth,* **126**, doi:10.1029/2020jb021125.

Mouzon, J., Bhuiyan, I. U. & Hedlund, J., 2016. The structure of montmorillonite gels revealed by sequential cryo-XHR-SEM imaging, *Journal of Colloid and Interface Science,* **465,** 58-66, doi:10.1016/j.jcis.2015.11.031.

Nagendrappa, G., 2011. Organic synthesis using clay and clay-supported catalysts, *Applied Clay Science,* **53,** 106-138, doi:10.1016/j.clay.2010.09.016.

Neuzil, C. E., 1994. How permeable are clays and shales?, *Water Resources Research,* **30,** 145-150, doi:10.1029/93wr02930.

O'Konski, C. T., 1960. Electric properties of macromolecules. V. Theory of ionic polarization in polyelectrolytes, *The Journal of Physical Chemistry,* **64,** 605-619, doi:10.1021/j100834a023.

Okay, G., Leroy, P., Ghorbani, A., Cosenza, P., Camerlynck, C., Cabrera, J., Florsch, N. & Revil, A., 2014. Spectral induced polarization of clay-sand mixtures: Experiments and modeling, *Geophysics,* **79,** E353-E375, doi:10.1190/Geo2013-0347.1.

Olhoeft, G. R., 1981. Electrical properties of rocks. *in Physical properties of rocks and minerals*, pp. 257–339, ed. Y. S. Touloukian, W. R. J., and R. F. Roy. McGraw-Hill, New York,

Parkhurst, D. L. & Appelo, C. A. J., 2013. 43 Description of Input and Examples for PHREEQC Version 3--a Computer Program for Speciation, Batch-reaction, One-dimensional Transport, and Inverse Geochemical Calculations. *in U.S. Geological Survey Techniques and Methods, Book 6, Modeling Techniques*, pp. 497, ed. Reston, U. S. G. S., Denver,

Pelton, W. H., Ward, S. H., Hallof, P. G., Sill, W. R. & Nelson, P. H., 1978. Mineral Discrimination and Removal of Inductive Coupling with Multifrequency-Ip, *Geophysics,* **43,** 588-609, doi:10.1190/1.1440839.

Petraglia, M. D., Ashton, N., Lewis, S. G., De Groote, I., Duffy, S. M., Bates, M., Bates, R., Hoare, P., Lewis, M., Parfitt, S. A., Peglar, S., Williams, C. & Stringer, C., 2014. Hominin Footprints from Early Pleistocene Deposits at Happisburgh, UK, *Plos One,* **9,** e88329, doi:10.1371/journal.pone.0088329.

Porté, J., Bretaudeau, F. & Girard, J. F., 2023. 3-D complex resistivity imaging using controlled source electromagnetic data: a multistage procedure using a second order polynomial parametrization, *Geophysical Journal International,* **233,** 839-860, doi:10.1093/gji/ggac486.

Pride, S., 1994. Governing Equations for the Coupled Electromagnetics and Acoustics of Porous-Media, *Physical Review B,* **50,** 15678-15696, doi:10.1103/PhysRevB.50.15678.

Qi, Y. & Wu, Y., 2022. Electrical Conductivity of Clayey Rocks and Soils: A Non-Linear Model, *Geophysical Research Letters,* **49**, doi:10.1029/2021gl097408.

Qi, Y. & Wu, Y., 2024. Induced Polarization of Clayey Rocks and Soils: Non-Linear Complex Conductivity Models, *Journal of Geophysical Research: Solid Earth,* **129**, doi:10.1029/2023jb028405.

Rasmusson, M., Rowlands, W., OBrien, R. W. & Hunter, R. J., 1997. The dynamic mobility and dielectric response of sodium bentonite, *Journal of Colloid and Interface Science,* **189,** 92-100, doi:10.1006/jcis.1997.4793.

Revil, A., 2012. Spectral induced polarization of shaly sands: Influence of the electrical double layer, *Water Resources Research,* **48,** 1-23, doi:10.1029/2011WR011260.

Revil, A., Cathles, L. M., Losh, S. & Nunn, J. A., 1998. Electrical conductivity in shaly sands with geophysical applications, *Journal of Geophysical Research-Solid Earth,* **103,** 23925-23936, doi:10.1029/98JB02125.

Revil, A. & Florsch, N., 2010. Determination of permeability from spectral induced polarization in granular media, *Geophysical Journal International,* **181,** 1480-1498, doi:10.1111/j.1365-246X.2010.04573.x.

Revil, A., Ghorbani, A., Jougnot, D. & Yven, B., 2023. Induced polarization of clay-rich materials — Part 1: The effect of desiccation, *Geophysics,* **88,** MR195-MR210, doi:10.1190/geo2022-0510.1.

Revil, A. & Glover, P. W. J., 1997. Theory of ionic-surface electrical conduction in porous media, *Physical Review B,* **55,** 1757-1773, doi:10.1103/PhysRevB.55.1757.

Revil, A. & Leroy, P., 2001. Hydroelectric coupling in a Clayey Material, *Geophysical Research Letters,* **28,** 1643-1646, doi:10.1029/2000GL012268.

Revil, A. & Leroy, P., 2004. Constitutive equations for ionic transport in porous shales, *Journal of Geophysical Research-Solid Earth,* **109,** 1-19, doi:10.1029/2003jb002755.

Revil, A., Leroy, P. & Titov, K., 2005. Characterization of transport properties of argillaceous sediments: Application to the Callovo-Oxfordian argillite, *Journal of Geophysical Research-Solid Earth,* **110,** B06202, doi:10.1029/2004jb003442.

Revil, A. & Linde, N., 2006. Chemico-electromechanical coupling in microporous media, *J Colloid Interface Sci,* **302,** 682-694, doi:10.1016/j.jcis.2006.06.051.

Revil, A. & Skold, M., 2011. Salinity dependence of spectral induced polarization in sands and sandstones, *Geophysical Journal International,* **187,** 813-824, doi:10.1111/j.1365-246X.2011.05181.x.

Richter, S. M. & Sevick-Muraca, E. M., 2000. Characterization of concentrated colloidal suspensions using time-dependent photon migration measurements, *Colloids and Surfaces A: Physicochemical and Engineering Aspects,* **172,** 163-173, doi:10.1016/s0927-7757(00)00581-1.

Robinson, D. A., 2004. Measurement of the solid dielectric permittivity of clay minerals and granular samples using a time domain reflectometry immersion method, *Vadose Zone Journal,* **3,** 705-713, doi:10.2136/vzj2004.0705.
Rotenberg, B., Cadéne, A., Dufrêche, J. F., Durand-Vidal, S., Badot, J. C. & Turq, P., 2005. An Analytical Model for Probing Ion Dynamics in Clays with Broadband Dielectric Spectroscopy, *The Journal of Physical Chemistry B,* **109,** 15548-15557, doi:10.1021/jp051586k.
Ruiz Pestana, L., Kolluri, K., Head-Gordon, T. & Lammers, L. N., 2016. Direct Exchange Mechanism for Interlayer Ions in Non-Swelling Clays, *Environmental Science & Technology,* **51,** 393-400, doi:10.1021/acs.est.6b04747.
Sahai, N. & Sverjensky, D. A., 1997. Evaluation of internally consistent parameters for the triple-layer model by the systematic analysis of oxide surface titration data, *Geochimica Et Cosmochimica Acta,* **61,** 2801-2826, doi:10.1016/S0016-7037(97)00128-2.
Schlumberger, C., 1920. *Study of underground electrical prospecting,* edn, Vol., Paris,
Schramm, L. L. & Kwak, J. C. T., 1982. Influence of Exchangeable Cation Composition on the Size and Shape of Montmorillonite Particles in Dilute Suspension, *Clays and Clay Minerals,* **30,** 40-48, doi:10.1346/Ccmn.1982.0300105.
Schroeder, P. A., 2018. *Clays in the Critical Zone,* edn, Vol., Cambridge University Press, Cambridge, UK, doi:10.1017/9781316480083.
Schurr, J. M., 1964. On the Theory of the Dielectric Dispersion of Spherical Colloidal Particles in Electrolyte Solution, *The Journal of Physical Chemistry,* **68,** 2407-2413, doi:10.1021/j100791a004.
Schwarz, G., 1962. A theory of the low-frequency dielectric dispersion of colloidal particles in electrolyte solution *The Journal of Physical Chemistry,* **66,** 2636-2642, doi:10.1021/j100818a067.
Secor, R. B. & Radke, C. J., 1985. Spillover of the diffuse double layer on montmorillonite particles, *Journal of Colloid and Interface Science,* **103,** 237-244, doi:10.1016/0021-9797(85)90096-7.
Sellin, P. & Leupin, O. X., 2013. The Use of Clay as an Engineered Barrier in Radioactive-Waste Management – A Review, *Clays and Clay Minerals,* **61,** 477-498, doi:10.1346/ccmn.2013.0610601.
Sen, P. N., 1984. Grain Shape Effects on Dielectric and Electrical-Properties of Rocks, *Geophysics,* **49,** 586-587, doi:10.1190/1.1441695.
Sen, P. N., Scala, C. & Cohen, M. H., 1981. A self-similar model for sedimentary rocks with application to the dielectric constant of fused glass beads, *Geophysics,* **46,** 781-795, doi:10.1190/1.1441215.
Sondi, I., Biscan, J. & Pravdic, V., 1996. Electrokinetics of pure clay minerals revisited, *Journal of Colloid and Interface Science,* **178,** 514-522, doi:10.1006/jcis.1996.0146.
Sposito, G., 1989. *The Chemistry of Soils* edn, Vol., Oxford University Press, New York,
Sposito, G., Skipper, N. T., Sutton, R., Park, S. h., Soper, A. K. & Greathouse, J. A., 1999. Surface geochemistry of the clay minerals, *Proceedings of the National Academy of Sciences,* **96,** 3358-3364, doi:10.1073/pnas.96.7.3358.
Tombacz, E. & Szekeres, M., 2004. Colloidal behavior of aqueous montmorillonite suspensions: the specific role of pH in the presence of indifferent electrolytes, *Applied Clay Science,* **27,** 75-94, doi:10.1016/j.clay.2004.01.001.
Tombacz, E. & Szekeres, M., 2006. Surface charge heterogeneity of kaolinite in aqueous suspension in comparison with montmorillonite, *Applied Clay Science,* **34,** 105-124, doi:10.1016/j.clay.2006.05.009.

Tournassat, C. & Appelo, C. A. J., 2011. Modelling approaches for anion-exclusion in compacted Na-bentonite, *Geochimica Et Cosmochimica Acta,* **75,** 3698-3710, doi:10.1016/j.gca.2011.04.001.

Tournassat, C., Bizi, M., Braibant, G. & Crouzet, C., 2011. Influence of montmorillonite tactoid size on Na-Ca cation exchange reactions, *Journal of Colloid and Interface Science,* **364,** 443-454, doi:10.1016/j.jcis.2011.07.039.

Tournassat, C., Bourg, I. C., Steefel, C. I. & Bergaya, F., 2015. Surface Properties of Clay Minerals, pp. 5-31, doi:10.1016/b978-0-08-100027-4.00001-2.

Tournassat, C., Chapron, Y., Leroy, P., Bizi, M. & Boulahya, F., 2009. Comparison of molecular dynamics simulations with triple layer and modified Gouy-Chapman models in a 0.1 M NaCl-montmorillonite system, *Journal of Colloid and Interface Science,* **339,** 533-541, doi:10.1016/j.jcis.2009.06.051.

Tournassat, C., Davis, J. A., Chiaberge, C., Grangeon, S. & Bourg, I. C., 2016a. Modeling the Acid–Base Properties of Montmorillonite Edge Surfaces, *Environmental Science & Technology,* **50,** 13436-13445, doi:10.1021/acs.est.6b04677.

Tournassat, C., Gaboreau, S., Robinet, J. C., Bourg, I. & Steefel, C. I., 2016b. Impact of microstructure on anion exclusion in compacted clay media, **22,** 137-149, doi:10.1346/cms-wls-21.11.

Tournassat, C., Grangeon, S., Leroy, P. & Giffaut, E., 2013. Modeling specific pH dependent sorption of divalent metals on montmorillonite surfaces. A review of pitfalls, recent achievements and current challenges, *American Journal of Science,* **313,** 395-451, doi:10.2475/05.2013.01.

Tournassat, C. & Steefel, C. I., 2019. Reactive Transport Modeling of Coupled Processes in Nanoporous Media, *Reviews in Mineralogy and Geochemistry,* **85,** 75-109, doi:10.2138/rmg.2019.85.4.

Triantafilis, J. & Lesch, S. M., 2005. Mapping clay content variation using electromagnetic induction techniques, *Computers and Electronics in Agriculture,* **46,** 203-237, doi:10.1016/j.compag.2004.11.006.

Udonne, J. D., 2011. A comparative study of recycling of used lubrication oils using distillation, acid and activated charcoal with clay methods, *Journal of Petroleum and Gas Engineering,* **2,** 12-19, doi:10.5897/JPGE.9000001.

Vandiver, P. B., Soffer, O., Klima, B. & Svoboda, J., 1989. The Origins of Ceramic Technology at Dolni Věstonice, Czechoslovakia, *Science,* **246,** 1002-1008, doi:10.1126/science.246.4933.1002.

Vinegar, H. J. & Waxman, M. H., 1984. Induced Polarization of Shaly Sands, *Geophysics,* **49,** 1267-1287, doi:10.1190/1.1441755.

Viseras, C., Carazo, E., Borrego-Sánchez, A., García-Villén, F., Sánchez-Espejo, R., Cerezo, P. & Aguzzi, C., 2019. Clay Minerals in Skin Drug Delivery, *Clays and Clay Minerals,* **67,** 59-71, doi:10.1007/s42860-018-0003-7.

Viseras, C., Cerezo, P., Sanchez, R., Salcedo, I. & Aguzzi, C., 2010. Current challenges in clay minerals for drug delivery, *Applied Clay Science,* **48,** 291-295, doi:10.1016/j.clay.2010.01.007.

Von Smoluchowski, M., 1905. Zur theorie der elektrischen kataphorese und der oberflachenleitung, *Physikalische Zeitschrift* **6,** 529-531.

Von Smoluchowski, M., 1921. edn, Vol. II, pp. 366-428, L. Graetz, Leipzig,

Wander, M. C. F. & Clark, A. E., 2008. Structural and Dielectric Properties of Quartz-Water Interfaces, *Journal of Physical Chemistry C,* **112,** 19986-19994, doi:10.1021/Jp803642c.

Waxman, M. H. & Smits, L. J. M., 1968. Electrical conductivities in oil bearing shaly sands, *Society of Petroleum Engineers Journal,* **8,** 107-122, doi:10.2118/1863-A.

Weller, A., Slater, L., Huisman, J. A., Esser, O. & Haegel, F. H., 2015. On the specific polarizability of sands and sand-clay mixtures, *Geophysics,* **80,** A57-A61, doi:10.1190/Geo2014-0509.1.

Weller, A., Slater, L. & Nordsiek, S., 2013. On the relationship between induced polarization and surface conductivity: Implications for petrophysical interpretation of electrical measurements, *Geophysics,* **78,** D315-D325, doi:10.1190/Geo2013-0076.1.

Xu, T., Sonnenthal, E., Spycher, N. & Pruess, K., 2006. TOUGHREACT—A simulation program for non-isothermal multiphase reactive geochemical transport in variably saturated geologic media: Applications to geothermal injectivity and CO2 geological sequestration, *Computers & Geosciences,* **32,** 145-165, doi:10.1016/j.cageo.2005.06.014.

Yang, D., Peng, S., Hartman, M. R., Gupton-Campolongo, T., Rice, E. J., Chang, A. K., Gu, Z., Lu, G. Q. & Luo, D., 2013. Enhanced transcription and translation in clay hydrogel and implications for early life evolution, *Sci Rep,* **3**, doi:10.1038/srep03165.

Yates, D. E., Levine, S. & Healy, T. W., 1974. Site-binding Model of the Electrical Double Layer at the Oxide/Water interface, *Journal of the Chemical Society, Faraday Transactions,* **70,** 1807-1818, doi:10.1039/F19747001807.

Yven, B., Sammartino, S., Geraud, Y., Homand, F. & Villieras, F., 2007. Mineralogy, texture and porosity of Callovo-Oxfordian argillites of the Meuse/Haute-Marne region (eastern Paris Basin), *Mémoires de la Société géologique de France,* **178,** 73-90.

Zhang, L., Lu, X., Liu, X., Zhou, J. & Zhou, H., 2014. Hydration and Mobility of Interlayer Ions of (Nax, Cay)-Montmorillonite: A Molecular Dynamics Study, *The Journal of Physical Chemistry C,* **118,** 29811-29821, doi:10.1021/jp508427c.

Zimmermann, E., Kemna, A., Berwix, J., Glaas, W., Munch, H. M. & Huisman, J. A., 2008. A high-accuracy impedance spectrometer for measuring sediments with low polarizability, *Measurement Science & Technology,* **19,** 105603, doi:10.1088/0957-0233/19/10/105603.

APPENDIX A. COMPUTED VOLUMES OF THE COMPONENTS OF THE CLAY MATERIAL

The volume of the solid part of the clay sample (not considering the interlayer space) (in m^3) is given by

$$V_s = \frac{10^{-3}\delta_s}{\rho_s}. \tag{A1}$$

The volumes of the solid part of the main clay mineral and of the remaining minerals in the sample are determined, respectively, from

$$V_{sc} = V_s \xi_c, \tag{A2}$$

$$V_{so} = V_s \left(1 - \xi_c\right), \tag{A3}$$

assuming that the minerals have roughly the same volumetric mass density.

The volume of the diffuse layer water is calculated using

$$V_w^d = S_o \chi_d, \tag{A4}$$

where S_o is the outer surface area of the main clay mineral in the mud (in m^2) and $\chi_d = 2\chi_D$.

The Debye length is calculated as a function of the bulk water chemical composition using

$$\chi_D = \sqrt{\frac{\varepsilon_w k_B T}{e^2 10^3 N_A \sum_{i=1}^{N} z_i^2 C_i^b}}. \tag{A5}$$

The quantity S_o in Eq. A4 is given by

$$S_o = \delta_{sc} S S_o, \tag{A6}$$

where $\delta_{sc} = \delta_s \xi_c$ is the solid mass of the main clay mineral in the mud (in g) and SS_o is the outer specific surface area of the main clay mineral in the mud (in $m^2\ g^{-1}$), which is computed using

$$SS_o = SS_e + \frac{SS_b}{n_c}, \tag{A7}$$

where n_c is the number of solid layers per clay particle (Tournassat *et al.* 2011). In Eq. A7, the SS_e quantity can be neglected for Mt and illite (see Section 2.1.).

The volume of the Stern layers is calculated using

$$V_S = S_o d_S, \tag{A8}$$

where d_S is the Stern layer thickness (in m) that can be approximated to 0.5 nm for the basal surface of illite and Mt (Bourg & Sposito 2011) and possibly to the same value for the edge surface (more work is necessary for the Stern layer modelling on the edge surface). Most of the time, the Stern layer volume can be neglected compared to the diffuse layer volume, but, in the case of compacted clays (dry density typically above 1600 kg m^{-3} (Massat *et al.* 2016)) and saline bulk aqueous solutions (ionic strengths typically ≥ 0.1 M (Leroy *et al.* 2015)), the diffuse layer can be highly compressed, and the Stern layer volume can be higher or equal to the diffuse layer volume and hence it cannot be neglected.

The volume of the interlayer space (for illite and Mt) is determined by

$$V_{in} = \frac{\delta_{sc} SS_b}{2n_c}(n_c - 1)t_{in}, \tag{A9}$$

where t_{in} is the thickness of the interlayer space (in m). The quantity $t_{in} \cong 10$ Å for Na-Mt and $t_{in} \cong 3$ Å for illite (crystal diameter of K^+ (Leroy *et al.* 2010)). But because K^+ ions are non-

solvated and for the mud we can take the mass of the clay powder containing already K^+ ions for V_s, we can assume $t_{in} \cong 0$ Å for illite (Tournassat *et al.* 2015) ($t_{in} \cong 0$ Å also for kaolinite).

Finally, the volume of bulk water is calculated according to the volume of the sample minus the estimated volumes of the other components of the mud:

$$V_w^b = V_t - V_s - V_w^d - V_S - V_{in} . \quad \text{(A10)}$$

APPENDIX B. COMPUTATION OF MODEL PARAMETER VALUES FROM TEMPERATURE AND SALINITY

In the model, the liquid water permittivity, for temperatures ranging from 2°C to 87°C (Lide 1990) and minus the decimal logarithm of the dissociation constant of water molecules ($pK_w = -\log K_w$), for temperatures ranging from 0°C to 100°C (Bandura & Lvov 2006), are computed as a function of the temperature in degree Celsius using

$$\varepsilon_w = \varepsilon_0 \left(a_0 + a_1 T_C + a_2 {T_C}^2 + a_3 {T_C}^3 \right), \quad \text{(B1)}$$

$$pK_w = b_0 + b_1 T_C + b_2 {T_C}^2 + b_3 {T_C}^3, \quad \text{(B2)}$$

where $a_0 = 87.895$, $a_1 = -4.0029 \times 10^{-1}$, $a_2 = 8.6132 \times 10^{-4}$, $a_3 = -9.565 \times 10^{-7}$, $b_0 = 14.95$, $b_1 = -4.38 \times 10^{-2}$, $b_2 = 2.32 \times 10^{-4}$, and $b_3 = -6.4 \times 10^{-7}$ in order to reproduce the related measurements.

The ion *i* mobility in bulk water at a temperature *T* (in K) is calculated from

$$T = T_C + 273.15, \tag{B3}$$

$$\beta_i^b(T) = \beta_i^b(298)\frac{T}{298}\frac{\eta_w(298)}{\eta_w}, \tag{B4}$$

where $\beta_i^b(298)$ is the ion *i* mobility in bulk water at a temperature of 298.15 K, $\eta_w(298)$ is the liquid water dynamic viscosity at a temperature of 298.15 K (~0.8905×10^{-3} Pa s), and η_w is the liquid water dynamic viscosity at a temperature *T*.

Ions of opposite charge decrease ion mobility in bulk water because of their mutual interaction (e.g., Bernard *et al.* 1992). Na^+ and Cl^- ion mobilities in bulk water at a temperature of 298.15 K are determined as a function of NaCl concentration in bulk water using

$$\beta_{Na^+}^b(298) = \left(a_0 + a_1 C_{NaCl}^b + a_2 {C_{NaCl}^b}^2\right)10^{-8}, \tag{B5}$$

for $C_{NaCl}^b \le 0.1\text{M}$,

$$\beta_{Na^+}^b(298) = \left(a_0' + a_1' C_{NaCl}^b\right)10^{-8}, \tag{B6}$$

for $C_{NaCl}^b > 0.1\text{M}$,

$$\beta_{Cl^-}^b(298) = \left(b_0 + b_1 C_{NaCl}^b + b_2 {C_{NaCl}^b}^2\right)10^{-8}, \tag{B7}$$

for $C_{NaCl}^b \le 0.1\text{M}$, and

$$\beta_{Cl^-}^b(298) = \left(b_0' + b_1' C_{NaCl}^b\right)10^{-8}, \tag{B8}$$

for $C_{NaCl}^b > 0.1\text{M}$,

where $a_0 = 5.07490$, $a_1 = -9.55617$, $a_2 = 7.73145$, $a_0' = 4.32333$, $a_1' = -1.07333$, $b_0 = 7.77572$, $b_1 = 10.77742$, $b_0' = 6.92256$, and $b_1' = 1.14556$ in order to reproduce the corresponding values simulated by the mean spherical approximation (MSA) method (Bernard *et al.* 1992; Leroy *et al.* 2015). For other types of ions (here H^+, OH^-, and Ca^{2+} and SO_4^{2-} ions from the interlayer space and dissolved clay minerals, according to Leroy *et al.* 2017b), we use for ion *i* mobility in bulk water

$$\beta_i^b(298) = \frac{\overline{D}_i^b(298)|q_i|}{k_B 298}, \tag{B9}$$

where $\overline{D}_i^b(298)$ is the measured ion *i* self-diffusion coefficient in distilled (bulk) water at a temperature of 298.15 K (in $m^2\ s^{-1}$) (Table B1 (Parkhurst & Appelo 2013)) (Eq. B9 is the Nernst-Einstein equation).

Table B1

Ion self-diffusion coefficient values in distilled water from the phreeqc.dat database

	Na^+	Cl^-	H^+	OH^-	Ca^{2+}	SO_4^{2-}
$\overline{D}_i^b(298)$ (10^{-9} m s^{-1})	1.33	2.03	9.31	5.27	0.793	1.07

In Eq. B3, the liquid water dynamic viscosity at a temperature T (in K) is computed from

$$\eta_w = \frac{\eta_w(293)}{10^{A/B}}, \tag{B10}$$

$$A = 1.37023(T - 293.15) + 8.36\times10^{-4}(T - 293.15)^2, \tag{B11}$$

$$B = T - 164.15, \tag{B12}$$

where $\eta_w(293)$ is the liquid water dynamic viscosity at a temperature of 293 K (~1.002×10^{-3} Pa s).

The ion mobility of the counter-ions in the Stern layer at a temperature T (K) is calculated from

$$\beta_S = \beta_S(298)\left[1+v_S\left(T-298.15\right)\right], \tag{B13}$$

$$\beta_S = \overline{\beta}_i^b(298)mr_S\left[1+v_S\left(T-298.15\right)\right], \tag{B14}$$

where $v_S = 0.037$ K^{-1} for sodium ion (Revil *et al.* 1998) (there are other v_S values for monovalent and divalent cations reported in Revil *et al.* 1998) and mr_S is the mobility ratio between a ion in the Stern layer and the same ion in bulk and distilled water at a temperature of 298.15 K (I is the ionic strength in M),

$$mr_S = \frac{\beta_S(298)}{\overline{\beta}_i^b(298)}, \tag{B15}$$

$$\overline{\beta}_i^b(298) = \lim_{I\to0}\beta_i^b(298), \tag{B16}$$

$$I = 0.5\sum_{i=1}^{N} z_i^2 C_i^b . \tag{B17}$$

The Stern layer of clays is mostly occupied by ions with the same sign of the charge. This is the reason why we use in Eqs B14 and B15 $\overline{\beta}_i^b(298)$ instead of $\beta_i^b(298)$. Indeed, because of the mutual interaction of anions and cations in bulk water, $\beta_i^b(298)$ decreases when salt concentration increases, which is not expected in the Stern layer of clays containing usually

mostly cations counter-ions. In our model, $\overline{\beta}_i^b(298)$ is a constant that is not decreasing with salinity on the contrary to $\beta_i^b(298)$.

APPENDIX C. COMPUTED BULK WATER CHEMICAL COMPOSITION

In our model, NaCl concentration in bulk water after evaporation, C_{NaCl}^b, is determined by:

$$C_{\mathrm{NaCl}}^b = C_{\mathrm{NaCl}}^0 \frac{\delta_t^0}{\delta_t^1}. \tag{C1}$$

HCl and NaOH electrolytes can also be added to NaCl electrolyte to change the pH. Hence, their concentrations after evaporation become

$$C_{\mathrm{HCl}}^b = C_{\mathrm{HCl}}^0 \frac{\delta_t^0}{\delta_t^1}, \tag{C2}$$

$$C_{\mathrm{NaOH}}^b = C_{\mathrm{NaOH}}^0 \frac{\delta_t^0}{\delta_t^1}. \tag{C3}$$

Ion concentrations in bulk water, C_i^b, are calculated according to:

$$a_{\mathrm{H^+}}^b = 10^{-\mathrm{pH}}, \tag{C4}$$

$$a_{\mathrm{OH^-}}^b = K_w / a_{\mathrm{H^+}}^b, \tag{C5}$$

$$C_{\mathrm{H^+}}^b \cong a_{\mathrm{H^+}}^b, \tag{C6}$$

$$C_{\mathrm{OH^-}}^b \cong a_{\mathrm{OH^-}}^b, \tag{C7}$$

$$C^b_{\mathrm{Cl^-}} = C^b_{\mathrm{NaCl}} + C^b_{\mathrm{HCl}} + \overline{C^b_{\mathrm{Cl^-}}}\,, \tag{C8}$$

$$C^b_{\mathrm{Na^+}} = C^b_{\mathrm{NaCl}} + C^b_{\mathrm{NaOH}} + \sum_i -z_i \overline{C^b_{i^{z_i+}}} + \sum_{i\neq j} z_j \overline{C^b_{j^{z_j-}}} - C^b_{\mathrm{H^+}} + C^b_{\mathrm{OH^-}} + C^b_{\mathrm{Cl^-}}\,, \tag{C9}$$

where $\overline{C^b_{i^{z_i+}}}$ and $\overline{C^b_{j^{z_j-}}}$ are ion (cation and anion) concentrations from dissolved minerals and Mt interlayer space. It should be noted that more complex electrolytes can be considered in our model, but here we focus on an electrolyte containing mostly Na^+, Cl^- and leached ions because we will show in Maineult *et al.* 2024) the comparison of our SIP model predictions to the corresponding measurements reported by Mendieta *et al.* (2021).

APPENDIX D. COMPUTED ELECTRICAL POTENTIAL AT THE *D*-PLANE AND SURFACE CONDUCTIVITY OF THE DIFFUSE LAYER

The φ_d potential is calculated by minimizing the following function:

$$\left|Q_{d1} - Q_{d2}\right| = 0\,, \tag{D1}$$

$$Q_{d1} = \sqrt{2\overline{\varepsilon_w} k_{\mathrm{B}} T 10^3 N_{\mathrm{A}} \sum_{i=1}^{N} C^b_i \left[\exp\left(-\frac{q_i \varphi_d}{k_{\mathrm{B}} T}\right) - 1\right]}\,, \tag{D2}$$

$$Q_{d2} = -Q_0\left(1 - f_Q\right), \tag{D3}$$

where Q_{d1} is the surface charge density of the diffuse layer calculated from the Gouy-Chapman theory (Hunter 1981) based on the assumption that the electrical potential in the diffuse layer does not change with the distance from the mineral surface at the end of the

diffuse layer, i.e. $\left(d\varphi / dx\right)_{x=\chi_d} = 0$ V m^{-1}. The expression of the surface charge density of the diffuse layer Q_{d2} (Eq. D3) was determined from

$$f_Q = \frac{Q_\beta}{Q_\beta + Q_{d2}}, \text{ and} \tag{D4}$$

$$Q_{d2} = -\left(Q_0 + Q_\beta\right), \tag{D5}$$

which make

$$f_Q = -\frac{Q_\beta}{Q_0}, \tag{D6}$$

and finally

$$Q_{d2} = -Q_0\left(1 - f_Q\right). \tag{D7}$$

Eq. D5 is the electroneutrality condition.

According to Schurr 1964, the low-frequency conductivity of a spherical particle of diameter *d* due to EDL polarisation and conduction is given by

$$\sigma_s = \frac{4}{d}\left(\Sigma_S \frac{i\omega\tau}{1+i\omega\tau} + \Sigma_s^d\right), \tag{D8}$$

where the first term in brackets represents conductivity from the polarisation of the bounded ion layer with surface conductivity Σ_S (in S) (Schwarz 1962) and the second term in brackets represents conductivity from ion electro-migration in the diffuse layer with surface conductivity Σ_s^d (Leroy *et al.* 2008).

Leroy *et al.* 2017b) showed that the first term in brackets of Eq. D8 significantly underestimates the complex conductivity magnitude of clay aggregates because it does not

consider the surface area of the clay particles inside the aggregate. To reproduce the measured Na-Mt complex conductivity magnitude, they therefore proposed to multiply this term by the ratio of the surface area of the clay particles inside the aggregate (S_o) to the surface area of the non-porous spherical particle with the same effective diameter d_k (S_k). We used the same method than Leroy *et al.* 2017b) to calculate aggregate conductivity considering EDL polarisation and conduction in the case here of a thin diffuse layer. After some algebraic developments, we obtained the following equation for aggregate conductivity

$$\sigma_s = \frac{2}{3}\phi_a \beta_S f_Q Q_V \frac{i\omega\tau}{1+i\omega\tau} - \frac{2}{3\vartheta}\phi_a \frac{\Sigma_s^d}{Q_0} Q_V \,. \tag{D9}$$

In Eq. D9, the surface conductivity of the diffuse layer can be calculated from

$$\Sigma_s^d = 10^3 N_A \int_0^{\chi_d} \left\{ \sum_{i=1}^{N} |q_i| \left[\beta_i^d C_i^d(x) - \beta_i^b C_i^b \right] + q_i C_i^d(x) \beta_{eo}^d(x) \right\} dx \,, \tag{D10}$$

where the first term of Eq. D10 represents diffuse layer surface conductivity due to ion electro-migration and the second term of Eq. D10 is diffuse layer surface conductivity due to electro-osmosis (Leroy *et al.* 2011). By assuming that ion concentration in the diffuse layer follows a Boltzmann's distribution, i.e. $C_i^d(x) = C_i^b \exp\left[-q_i\varphi(x)/k_B T\right]$ and that ion mobility in the diffuse layer is equal to ion mobility in bulk water, i.e. $\beta_i^d = \beta_i^b$, and using Eq. 29, Eq. D10 reduces to

$$\Sigma_s^d = 10^3 N_A \int_0^{\chi_d} \left\{ \sum_{i=1}^{N} |q_i| \beta_i^b C_i^b \left\{ \exp\left[-\frac{q_i\varphi(x)}{k_B T} \right] - 1 \right\} + q_i C_i^b \exp\left[-\frac{q_i\varphi(x)}{k_B T} \right] \frac{\overline{\varepsilon_w}}{\eta_w} \left[\varphi(x) - \varphi_d \right] \right\} dx \,, \tag{D11}$$

where the electrical potential distribution in the diffuse layer $\varphi(x)$ is given by Eq. 37 or Eq. 38.

According to Revil & Glover 1997), Eq. D11can be simplified to

$$\Sigma_s^d = \chi_d 10^3 N_A \sum_{i=1}^{N} |q_i| B_i^d C_i^b \left[\exp\left(-\frac{q_i \varphi_d}{2 k_B T} \right) - 1 \right], \tag{D12}$$

$$B_i^d = \beta_i^b + m_i^d, \tag{D13}$$

where m_i^d (in $m^2\ s^{-1}\ V^{-1}$) in Eq. D13 is related to the increase of electrical conductivity of the diffuse layer due to electro-osmosis (Bikerman 1940; Revil & Glover 1997; Leroy *et al.* 2011). The term m_i^d is written as

$$m_i^d = \frac{2 \overline{\varepsilon_w} k_B T}{\eta_w |q_i|}. \tag{D14}$$

Eqs D12-D14 have been developed considering a symmetric electrolyte where cation valence z_+ is equal to anion valence z_- (Pride 1994; Lyklema & Minor 1998). In the case of an asymmetric electrolyte, Eqs D12-D14 can be used to compute the diffuse layer surface conductivity despite being more approximate than in the case of a symmetric electrolyte (Revil & Glover 1997). Eqs D12-D14 are strictly valid for $|\varphi_d| < k_B T / (ze)$ where z is the valence of the symmetric electrolyte ($k_B T / e \cong 25.7\,\text{mV}$ at a temperature of 298.15 K). Indeed, they are based on the Debye-Hückel (D-H) approximation, i.e. $|\varphi| << k_B T / (ze)$, to compute the electrical potential distribution in the diffuse layer from the φ_d potential and the Poisson-Boltzmann (P-B) equation, i.e. $\varphi(x) = \varphi_d \exp(-x / \chi_d)$ (Hunter 1981; Pride 1994). In our model, we consider that the diffuse layer can contribute to the surface conductivity of the aggregate when the diffuse layer is thinner than the particle. For illite and Mt, this occurs

typically when the diffuse layer is highly compressed (see end of section 3.3) at high ionic strengths typically ≥ 0.1 M where the φ_d potential magnitude should be low satisfying $|\varphi_d| < k_B T/(ze)$ (Sondi *et al.* 1996; Leroy *et al.* 2015). Therefore, in this condition, Eqs D12-D14 are valid for our calculation of the surface conductivity of the diffuse layer within the aggregate. It should be noted that Eq. D11 with Eq. 37 or 38 or Eqs D12-D14 can be used to compute the diffuse layer surface conductivity of kaolinite and illite particles at typically lower ionic strengths than Mt particles because kaolinite and in a lesser extent illite particles are thicker than Na-Mt particles and they do not have interlayer space containing hydrated and mobile cations.

If the ion mobilities are similar in the diffuse layer, Eq. D12 can be reduced to

$$\Sigma_s^d = B_d Q_d , \tag{D15}$$

and Eq. D9 finally becomes

$$\sigma_s = \frac{2}{3}\phi_a \left[\beta_S f_Q \frac{i\omega\tau}{1+i\omega\tau} + \frac{B_d}{\vartheta}\left(1-f_Q\right)\right] Q_V , \tag{D16}$$

$$\sigma_s = \frac{2}{3}\phi_a \left[\beta_S f_Q \frac{i\omega\tau}{1+i\omega\tau} + \widetilde{B_d}\left(1-f_Q\right)\right] Q_V . \tag{D17}$$

The ϑ ratio can be computed using Eq. A6

$$\vartheta = \frac{S_o}{S_k} = \frac{\delta_{sc} S S_o}{\pi d_k^{\,2}} . \tag{D18}$$

APPENDIX E. COMPUTED AVERAGE ELECTRICAL POTENTIAL IN THE DIFFUSE LAYER AND INTERLAYER SPACE OF NA-MT

We use the volume averaging method to compute φ_m as a function of CEC and bulk water chemical composition (Revil & Leroy 2004; Leroy *et al.* 2007; Leroy *et al.* 2017b). We assume that the (usually negative) surface charge of the clay mineral is compensated by the excess of counter-charge per unit pore volume in the Stern and diffuse layers and interlayer space of Na-Mt, i.e.

$$\frac{1}{V_t}\left(\int_0^{S_{in}} Q_0 dS + \int_0^{V_{in}} Q_V^{in} dV + \int_0^{S_o} Q_0 dS + \int_0^{V_S+V_w^d} Q_V^o dV \right) = 0 , \tag{E1}$$

where S_{in} is the surface area of the interlayer space (in m^2), Q_V^{in} is the excess of charge per unit interlayer space volume (in C m^{-3}) and Q_V^o is the excess of charge per unit Stern and diffuse layer volumes. In the case of kaolinite and illite, the first two terms in Eq. E1 can be assumed to be zero (no interlayer space and interlayer space containing non-solvated K^+ ions, respectively). In the case of Na-Mt, we assume that $Q_V^{in} = Q_V^o$. Eq. E1 then becomes

$$\frac{1}{V_t}\left(\int_0^{S_{in}+S_o} Q_0 dS + \int_0^{V_{in}+V_S+V_w^d} Q_V^o dV \right) = 0 . \tag{E2}$$

If Q_0 and Q_V^o are assumed constant throughout the pore surface and volume, respectively, and, according to Eq. A6, Eq. E2 simplifies to:

$$Q_V^o = -\frac{\delta_{sc} SS}{V_{in}+V_S+V_w^d} Q_0 , \tag{E3}$$

for Na-Mt, and

$$Q_V^o = -\frac{\delta_{sc} SS}{V_S + V_w^d} Q_0 \,, \tag{E4}$$

1666 for kaolinite and illite. The excess of charge per unit pore volume in the diffuse layer and
1667 interlayer space of Na-Mt (contributing solely to conduction due to ion electro-migration) is
1668 written as:

$$Q_V^d = 10^3 N_{\mathrm{A}} \sum_{i=1}^{N} q_i \overline{C_i^d} \,, \tag{E5}$$

$$Q_V^d = (1 - f_Q) Q_V^o \,, \tag{E6}$$

1669 and, finally, using Eqs E3, E5, and E6 for Na-Mt and Eqs E4, E5, and E6 for kaolinite and
1670 illite, the φ_m potential was computed from

$$10^3 N_{\mathrm{A}} \sum_{i=1}^{N} q_i C_i^b \exp\left(-\frac{q_i \varphi_m}{k_{\mathrm{B}} T}\right) + (1 - f_Q) \frac{\delta_{sc} SS}{V_{in} + V_S + V_w^d} Q_0 = 0 \,, \tag{E7}$$

1671 for Na-Mt, and

$$10^3 N_{\mathrm{A}} \sum_{i=1}^{N} q_i C_i^b \exp\left(-\frac{q_i \varphi_m}{k_{\mathrm{B}} T}\right) + (1 - f_Q) \frac{\delta_{sc} SS}{V_S + V_w^d} Q_0 = 0 \,, \tag{E8}$$

1672 for kaolinite and illite, where $\overline{C_i^d} = C_i^b \exp\left(-q_i \varphi_m / k_{\mathrm{B}} T\right)$ is the average ion concentration in
1673 the diffuse layer and interlayer space of Na-Mt or in the diffuse layer of kaolinite and illite,
1674 which follows a Boltzmann's distribution. The Q_0 quantity is expressed as a function of CEC
1675 using Eq. 14. We assume in Eq. E7 that the interlayer space of Na-Mt behaves like the EDL
1676 on the clay external surface. This assumption could be considered rather crude but we do not
1677 want to complicate more our model and hence add additional parameter values to be fitted in
1678 our model.
1679